RESEARCH ARTICLE

Optimization and performance of metafoundations for seismic isolation of small modular reactors

Tugberk Guner[1] | **Oreste S. Bursi[1]** | **Silvano Erlicher[2]**

[1]Department of Civil, Environmental and Mechanical Engineering, University of Trento, Trento, Italy

[2]EGIS Nuclear Activity, Business Line GO3E, EGIS GROUP, Montreuil, France

Correspondence
Oreste S. Bursi, Department of Civil, Environmental and Mechanical Engineering, University of Trento, Via Mesiano, 77, 38123, Italy.
Email: oreste.bursi@unitn.it

Abstract

This paper aims to study the seismic mitigation of a typical nuclear small modular reactor (SMR) where extreme loading conditions are considered by the safe shutdown earthquake. For this purpose, to reproduce the main dynamic properties of the reactor's reinforced concrete system, a detailed structural model was synthetized, also taking into account the presence of the reactor pools. Thus, to protect the reactor from strong earthquakes, finite locally resonant multiple degrees of freedom metafoundations were developed; and resonator parameters were optimized by means of an improved frequency domain multivariate and multiobjective optimization procedure. Also, the stochastic nature of the seismic input was taken into account. It is proposed: (i) a linear metafoundation endowed with multiple cells, linear springs, and linear viscous dampers; and (ii) a foundation equipped with additional nonlinear vertical quasi-zero stiffness (QZS) cells. QZS cells were obtained by horizontally precompressed springs in an unstable state with vertical springs in parallel. With this arrangement, additional flexibility and dissipation against nonsymmetrical modes of the SMR and vertical seismic loadings are proposed. It was shown in both cases, how each metafoundation was successfully optimized via a sensitivity-based parameter grouping strategy and a hybrid grid searching algorithm. Thus, the performance of the optimized metafoundations was assessed by means of frequency and time history analyses; and finally, results were compared with an SMR endowed with both rigid foundation and conventional base-isolation solutions.

1 | INTRODUCTION

1.1 | Background and motivations

The Fukushima earthquake of March 11, 2011, occurred in Japan and clearly showed that nuclear power plants (NPPs) can face extreme actions and be subjected to nuclear disasters.

These unfavorable events may create significant concern for NPPs in high seismicity regions even though all precautions and safety regulations are followed. Then, many studies have been conducted and Stevenson (2014), among others, showed that the March 11 earthquake in Japan exerted limited seismic effects on nuclear reactor structures despite the large magnitude $M_w = 9.0$ recorded. The wave effects of the consequent tsunami were higher than

the historical records, and this led to full flooding of both the adjacent area and the power plant (Anawat et al., 2013). This sequence of events triggered the Fukushima Dai-ichi disaster with the hydrogen explosion in the reactor buildings—Unit #1 and #3—and around the torus—Unit #2—due to insufficient cooling provided by the emergency diesel generators caused by a lack of power supply (IAEA, 2016; Synolakis & Kânoğlu, 2018). As a result, the damage at the Fukushima NPP entailed intensive research and engineering efforts to include safe shutdown earthquakes (SSEs), not foreseen in the original design (Furuta & Kanno, 2017; Park & Seol, 2016). This justifies the need to consider other earthquake levels stronger than those used in the SSE, that is, 0.3 g, at least at the simulation level.

In recent years, the next generation of nuclear power reactors has been developed worldwide. Thus, both small and medium reactors endowed with a typical maximum output capacity of around 300 and 700 MWe are available (IAEA, 2014). They exhibit many superior advantages with regard to previous solutions in terms of safety, high manufacturing quality, power scalability, and economic affordability (Upadhyay et al., 2003). More specifically, to satisfy future energy demands, small modular reactors (SMRs) gained a lot of interest in governmental agencies as well as in the research community due to their different sizes and high flexibility. As nuclear power research in Europe is mostly slowed down by political indecision and people's concern over NPPs and their capability to face extreme natural events with limited damage, it is worthwhile to study in-depth the archetype of integral pressurized water reactor from the NuScale design and to examine its structural response this reactor would have in the case of a large seismic event similar to those of 2011 in Japan. In particular, there is an interest in its seismic performance along the main vein of the technological progress made in the field of seismic passive control, that is, dissipation and isolation (El-Khoury & Adeli, 2013; Gutierrez Soto & Adeli, 2018).

With regard to seismic risk assessment procedures for NPPs, new procedures for probabilistic seismic risk assessment were proposed (Y.-N. Huang et al., 2011a). They used tools recently developed for performance-based earthquake engineering of buildings. In particular, the use of response rather than ground motion-based fragility curves enabled the curves to be independent of seismic hazard and closely related to component capacity. These tools were successfully applied to a sample NPP reactor building (Y.-N. Huang et al., 2011b).

Concerning the seismic isolation of nuclear reactors, different research aspects were investigated in depth. An important issue was the effect of mainshock–aftershock sequences. In this respect, Zhao et al. (2019) analyzed a 3D finite element (FE) model of an isolated AP1000 NPP building under different mainshock–aftershock sequences

and conducted a parametric analysis. Relevant results indicated that aftershocks have a small impact on the seismic performance of the isolated nuclear building. Mainshocks and aftershocks also influence the horizontal floor response spectra and the stress state to some extent; however, effects are relatively minor, compared to the nonisolated building.

Considering experimental activities, Shellenberg et al. (2015) were able to conduct hybrid simulations of an APR-1400 NPP. A realistic numerical FE model of the superstructure was coupled to two types of isolation systems, that is, one based on lead plug rubber bearings and the other based on friction bearings with one or two horizontal components of a ground motion, as well as considering the vertical component of the excitation. These hybrid simulations revealed the ability of the seismic isolation systems utilized to perform well under design conditions; the tests also revealed that both of the bearing types tested showed substantial vertical–horizontal coupling. While this behavior had a negligible effect on bearing displacement demands, it had a significant effect on the floor response spectra. In this respect, Y.-N. Huang et al. (2016) clearly showed and quantified the correlation between vertical and horizontal components of strong ground motions on the basis of records coming from a database compiled for large-magnitude shallow crustal earthquakes.

Along the same vein, that is, the protection of NPPs components against the vertical component of the earthquake, Fukasawa et al. (2019) proposed a new 3D complex isolator consisting of rubber bearings, vertical oil dampers, and disc spring units. In addition, Najafijozani et al. (2020), proposed other six systems based on adaptive control and consisted of in-parallel configurations of linear and nonlinear springs and dampers. The peak isolation displacement and peak equipment acceleration were used to assess the effectiveness of the vertical isolation systems.

As far as seismic isolation standards are concerned, the Japanese technical guidelines related to the design of NPPs (JEAG4614, 2013) clearly indicated the need for safety margins to favor the linear behavior of laminated rubber bearings to be used in strong earthquake-prone zones. In this respect, also Parsi et al. (2022) promoted the standardization of advanced reactor designs. Thus, the adoption of seismic isolation can exploit a site-independent certified design and repeated acquisition of safety-class equipment. The standardized designs based on seismic isolation are demonstrated for two different advanced reactors based on molten salt and high-temperature gas.

As an alternative to classical seismic isolation for earthquake mitigation, a new category of applications of periodic materials is steadily receiving growing

interest (Mu et al., 2020; Muhammad & Lim, 2022). Their popularity stems from the possibility of exploiting the advantages of periodicity that can attenuate or practically suppress waves in certain frequency ranges. With reference to the seismic mitigation of process equipment, Basone et al. (2019), Wenzel et al. (2020), and Bursi et al. (2021) clearly showed the advantages of locally resonant metamaterials in metafoundations endowed with linear and nonlinear springs, respectively. Optimized metafoundations endowed with isolation and dissipation capabilities mitigated low-frequency seismic waves. In this respect, linear/nonlinear unit cells were conceived to be much smaller than the wavelength of the wanted frequency region. Differently from most standard isolation solutions, such as lead-rubber bearings or spherical bearing devices, metafoundations do not require two strong floors; and more, they are also effective against the vertical component of earthquakes (Franchini et al., 2020).

Regarding the seismic isolation of NPP by means of metamaterials, the research work of Witarto et al. (2018, 2019) is deemed to be mentioned. In the first work, the authors designed a 1D periodic foundation made of reinforced concrete (RC) and polyurethane; thus, based on frequency-band-gap properties, they attenuated waves in both the horizontal and vertical directions together with the torsional mode. Furthermore, when the frequencies of the incoming waves were within the frequency band gaps, the 1D periodic foundation isolated the superstructure with a limited relative displacement. Experimental verification was conducted on a shaking table with a 1/22 scaled mock-up. Clearly, the scaling attenuates potential problems of polyurethane layers. A similar metafoundation was designed in the second research paper where the same materials have been used and arranged in the form of cubes. Only one layer of cells with resonators made of concrete was used, and cells were used for both horizontal and vertical excitations. Nonetheless, owing to the presence of polyurethane, possible damage due to exceptional fire action should be accounted for.

Also, in the context of NPPs coupled with metafoundations, two basic issues remained unresolved: (i) the reduction of the vertical component of an earthquake and associated rocking due to structural asymmetry; (ii) the optimization of structural devices, that is, springs and/or dampers, operating in the linear/nonlinear regime within finite lattices for coupled horizontal and vertical seismic excitation. As far as the first issue is concerned, it is worthwhile, to take benefit from the so-called conceptual quasi-zero stiffness (QZS) elements inserted in resonators of mass-in-mass periodic systems (Lin et al., 2021; Shi et al., 2021). More precisely, to effectively damp out vibrations in the low-frequency regime, each QZS element exerts a high static and low dynamic stiffness characteristic. In practice, the QZS elements are realized by the parallel connection of positive and negative stiffness elements. For instance, Carrella et al. (2009) developed a classical QZS isolator by means of linear and nonlinear oblique springs and systematically studied its static and dynamic characteristics.

Regarding the second issue, the nonlinear multivariate optimization problem can be solved using both deterministic methods and/or heuristic methods. A review of deterministic methods in structural optimization studies can be found in Sarma and Adeli (1998). In particular, the pattern search method (Hooke & Jeeves, 1961) and the simplex method (Nelder & Mead, 1965) require an initial solution guess; the golden section search (GSS) algorithm and its derivations (Chang, 2009) instead require only boundaries. Although deterministic methods are efficient, they tend to fall into local extrema. Conversely, heuristic methods use probabilistic transition rules for global optimum search, and their process is inspired by nature (Aldwaik & Adeli, 2014). In structural optimization, among others, one can cite genetic algorithms (GAs; Kicinger et al., 2005), particle swarm optimization (PSO; Shafahi & Bagherian, 2013) and simulated annealing (SA; Paya et al., 2008). As regards the solution of multi-objective optimization, a set of optimal solutions, the Pareto front, can be obtained (Ruy et al., 2001). Nonetheless, especially when it is difficult to select the best solution, one common approach is to use the weighted sum method (WSM), to synthesize one single objective function that can be solved using the aforementioned methods (Marler & Arora, 2010). Generally, the weights are determined by decision-makers.

1.2 | Scope

This study aims to develop and evaluate two types of metafoundations for the seismic protection of a NuScale-type SMR building, hereinafter shortly called SMR, for both horizontal and vertical excitations. The metafoundations differ from the previous ones conceived by Basone et al. (2019) and Bursi et al. (2021) for two fundamental reasons: (i) the optimization procedure of the metafoundations both for horizontal and vertical components of the earthquake; (ii) the proper utilization of QZS elements conceived to add vertical flexibility. To reduce computational expense and focus on more important aspects, the main dynamic properties of the SMR were retained only in the X and Z directions with rotational coupling. Hence, modeling and analyses were conducted considering a 2D X-Z plane.

More precisely, the first type of metafoundation, the so-called linear metafoundation (LM), contains a layer

COMPUTER-AIDED CIVIL AND INFRASTRUCTURE ENGINEERING

of locally resonant linear unit cells. The second type of metafoundation instead, the so-called metafoundation with QZS layers (QM), contains single or multiple layers consisting of QZS unit cells, in addition to a layer of linear unit cells. Each QZS unit cell exhibits vertical high-static low-dynamic stiffness, which is obtained by horizontally precompressed springs in an unstable state with vertical positive springs in parallel.

Primarily, the following objectives are pursued: (i) modeling of the SMR by means of a low-fidelity model that includes the internal fluid presence of the reactor pools; (ii) discrete modeling and code-compliant design of LM and QMs; (iii) development of an efficient deterministic optimization procedure to define optimum resonator parameters of metafoundations; (iv) performance assessment of the metafoundations in both frequency and time domains.

Along these lines, the metafoundations were designed to remain undamaged at an active seismic site characterized by 0.3 g at SSE (ASCE/SEI, 2016) located in Priolo Gargallo, Sicily, Italy. For the vertical component of the earthquake, instead, a peak ground acceleration (PGA) of 0.2 g was adopted (Y.-N. Huang et al., 2016).

The paper is organized as follows. First, the details of the SMR and the relevant modal reduction are provided in Section 2. Section 3 describes the details of the novel proposed metafoundation unit cells. Both the modeling and design of the metafoundations are presented in Section 4. The proposed optimization procedure for the resonator parameters is presented in Section 5. In Section 6, the performance of the optimized systems is verified by means of the SMR displacement and acceleration responses obtained from nonlinear time history analyses (THA) with relevant advantages. Finally, conclusions and future developments are presented in Section 7.

2 | DESCRIPTION OF THE SMR

The schematic of the SMR is given in Figure 1a and includes RC walls and slabs, containment pools, and reactor modules. The building can contain and operate up to 12 compact reactor modules simultaneously. Each module is 25-m tall with a diameter of 4.6 m, and it is expected to produce up to 77 MWe gross electric power; all modules in operation provide up to 924 MWe gross power (Benefits NuScale Power, 2022). All reactor modules are self-contained integral reactors placed in a common large water pool, named the reactor pool. In addition, to cool down the used fuel, the building contains a smaller water pool, the so-called spent fuel storage pool.

The RC structure of the SMR consists of RC walls with a 0.75–1 m thickness and slabs with a 0.5 m thickness. As

shown in Figure 1b, the total width of the building reaches 76 m with a depth of 30 m. The total height of the SMR is 40 m; however, to minimize the effects of impact-type loads such as airplane crashes or explosions, it is buried underground for 25 m. The total mass of the SMR amount to 117,700 tons when at the operational level, the pools are full. The main views and finer details can be found in a few documents; see, among others, IAEA (2014).

To evaluate the modal properties of the SMR, experimental data were not available (Amezquita-Sanchez et al., 2017); thus, for analysis purposes, the RC components of the SMR were modeled by means of the FE software SAP2000 with quadrilateral shell elements (CSI, 2022). Since the soil was characterized by small deformations, the base slab was directly connected to the ground by means of fixed restraints. The masses associated with the reactor modules were also included using point masses with rigid links. The modal properties of the first 10 modes provided from modal analysis are presented in Table 1; they involve the highest mass participation (MP) ratios in horizontal, vertical, and rotational directions.

The deformed configurations relevant to the main modes can be observed in Figure 1c. The total MP ratios of the computed modes reach above 90% in the horizontal and 84% in vertical directions, which is sufficient to represent the dynamic characteristics of the structure (Chopra, 2017).

It is worthy to recall the research focus, that is, to prove the efficacy of seismic mitigation properties of both the optimized LM and the QM and the FE model of the SMR. Thus, the FE model was further reduced to a 3 degrees of freedom (DoF)—horizontal, vertical, and rotational—system low-fidelity lumped mass model. With this objective in mind, both the MP factors and the fundamental frequencies of the first 10 modes collected in Table 1 are used for dynamic reduction. Thus, based on the generalized eigenvalue problem (Golub & Van Loan, 2012),

$$\mathbf{K_S} \cdot \mathbf{\Phi} = \mathbf{M_S} \cdot \mathbf{\Phi} \cdot \mathbf{\Omega}^2 \qquad (1)$$

One can identify the two symmetric matrices $\mathbf{K_s}$ and $\mathbf{M_s} \in \mathbb{R}^{d \times d}$ where: d indicates the retained DoFs, that is, 3; $\mathbf{K_s}$ and $\mathbf{M_s}$ define the stiffness and the mass matrix of the reduced model. In addition, one can express $\mathbf{\Phi}$ and $\mathbf{\Omega}$ as

$$\mathbf{\Phi} = Y_{3\times n} = \begin{bmatrix} Y_{11} & \cdots & Y_{1n} \\ \vdots & \ddots & \vdots \\ Y_{31} & \cdots & Y_{3n} \end{bmatrix} \mathbf{\Omega}^2 = \begin{bmatrix} \omega_1^2 & & \\ & \ddots & \\ & & \omega_n^2 \end{bmatrix} \qquad (2)$$

where $Y_{3\times n}$ is the matrix of MP ratios of the first nth modes and ω_n define the frequency of the nth mode. As a result, the horizontal and vertical equivalent frequencies
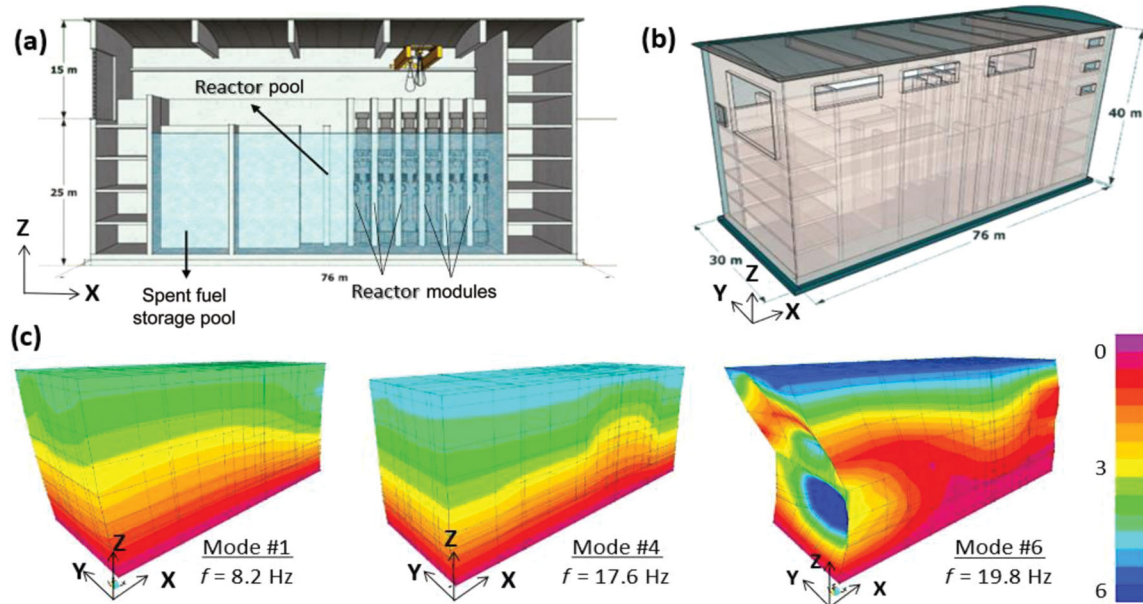
FIGURE 1 Schematic of the small modular reactor (SMR) and finite element modal analysis results: (a) inner view; (b) outer view; (c) deformed shapes relevant to Modes 1, 4, and 6

TABLE 1 Modal properties and mass participation (MP) ratios of the small modular reactor finite element model

Mode	Freq. (Hz)	Horizontal MP (%)	Vertical MP (%)	Rotational MP (%)
1	8.2	82.7	0.00	7.69
2	14.2	0.58	1.42	2.02
3	15.3	5.86	0.16	5.61
4	17.6	0.01	81.6	0.45
5	18.4	0.03	0.10	0.52
6	19.8	1.29	1.00	8.51
7	20.3	0.30	0.13	2.09
8	21.2	0.00	0.00	0.11
9	22.9	1.34	0.00	1.05
10	23.6	0.02	0.04	0.37
	Total:	**92.1**	**84.5**	**28.4**

of the reduced model read 8.2 and 17.6 Hz, respectively, while the rotational stiffness is estimated as 18.2 Hz. Note that the first two frequencies match with the first and the fourth frequencies of Table 1. The resulting 3×3 coupled stiffness matrix $\mathbf{K_s}$ is symmetric and full.

Regarding the damping ratio, the document NUREG/CR-7193(2015) indicates that values provided by the Regulatory Guide 1.61 (U.S. Nuclear Regulatory Commission, 2007) are valid for conventional NPPs but unsuitable for the smaller size and mass of an SMR. Consequently, a damping ratio of 3% valid for RC structures was selected (Chopra, 2017).

The water pools were also introduced to the reduced model. In the horizontal direction, following Graham and Rodriguez (1952), both the rectangular reactor pool and

the spent fuel storage pools were simulated by dynamic masses and stiffnesses. Conversely, the model proposed by Veletsos and Tang (1986) was applied to the total mass of the two pools for actions in the vertical direction. Therefore, for each pool, 2 DoFs for the horizontal components were introduced. In addition, 2 DoFs for the vertical component of both pools were considered. It must be emphasized that the simplified models of the pools also contribute to the rotational response of the SMR model. Initially, both simplified models neglected the damping ratio of water, and damping was assigned to walls. Since damping values greater than zero improve computational convergence, a damping ratio of 1% was considered for the pool masses and their contribution to the rotational response.
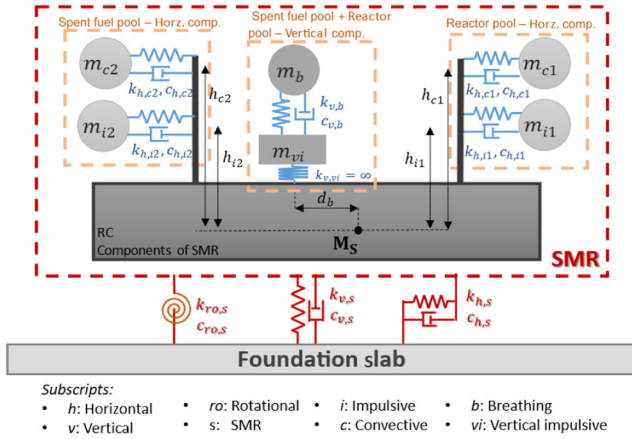
WILEY $\mid$ **1563**

FIGURE 2 Coupled spring-mass model of the SMR building

The final spring-mass model of the SMR is depicted in Figure 2. The dashed line box represents the reduced model together with the simplified pool models. The pool masses m_{i1}, m_{i2}, m_{c1}, m_{c2}, m_b, and m_{vi} connect to the reduced model mass $\mathbf{M_s} = \text{diag}(m_s, m_s, I_s)$ but do not connect to the foundation slab. The subscripts i, c, b, and vi correspond to impulsive, convective, breathing, and vertical impulsive mass terms, respectively. The given horizontal–vertical–rotational spring triplets that connect the masses of $\mathbf{M_s}$ to the foundation slab are coupled but, for clarity, they have separately been drawn. The foundation slab depicted in Figure 2 represents a schematic foundation; clearly, it can be replaced by a rigid foundation (RF) or the optimized LM/QM. In parallel with Figure 2, a 9×9 diagonal mass matrix $\mathbf{M_{SMR}}$ and the symmetric stiffness matrix $\mathbf{K_{SMR}}$ of the complete SMR can be assembled.

3 | CHARACTERISTICS OF THE UNIT CELLS

The anticipated metafoundations utilize two different types of cells: (i) locally resonant linear unit cells, and (ii) QZS unit cells. For brevity, the—locally resonant—nomenclature is not used in the rest of the paper. The details and the underlying dynamics of these cells are explained herein.

3.1 | The linear unit cell

The schematic of the linear unit cell is provided in Figure 3. More precisely, each unit cell is characterized by 5-m width and 5-m depth and variable column height, H. Given the size of the SMR, the LM comprises a single-linear-layer with a lattice of $15 \times 6 = 90$ linear unit cells. The modularity and flexibility of these cells are evident. More pre-
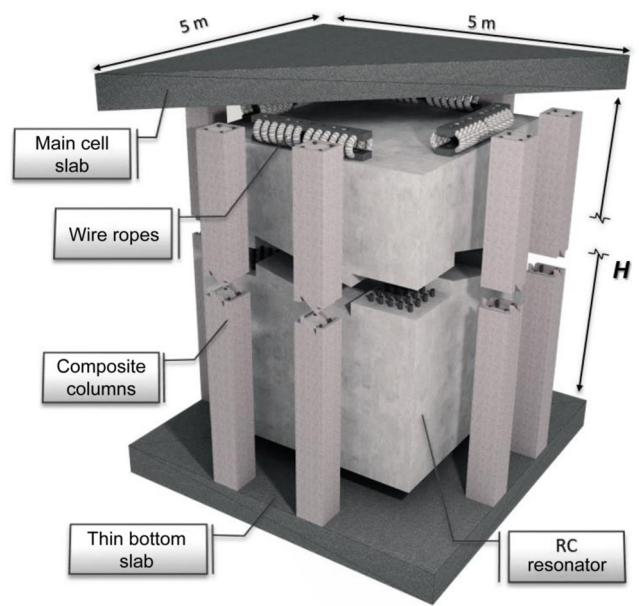

FIGURE 3 Schematic of the linear unit cell sectioned at mid-height to provide an inside view of the reinforcement layout. Dimensions of elements are not to scale. RC, reinforced concrete

cisely, each unit cell depicted in Figure 3 contains two main parts: the main exterior cell and the massive resonator. The main cell comprises the slab and the composite columns that connect the RC slab to the ground foundation. Also, the resonators are made of RC and are connected to the RC slab with wire ropes. In detail, wire ropes exhibit a nonlinear coupled dynamic behavior as reported in Alessandri et al. (2015). However, Basone et al. (2021) and Bursi et al. (2021) clearly showed that in monodirectional cases and limited displacements, the wire ropes can be modeled as linear spring-damper devices without introducing significant errors. As a result, the wire ropes were modeled as linear springs and dampers. Hence, the stiffness and damping parameters of the resonators read,

$$k_{h,r} = m_r \omega_{h,r}^2 \quad c_{h,r} = 2\zeta_{h,r} m_r \omega_{h,r}$$
$$k_{v,r} = m_r \omega_{v,r}^2 \quad c_{v,r} = 2\zeta_{v,r} m_r \omega_{v,r} \quad (3)$$

where ω and ζ correspond to the frequency and damping ratios, while subscript h, v, and r are used for horizontal, vertical, and resonator terms, respectively.

The linear unit cells rely on the combination of two important aspects conceived to reduce displacements/accelerations at the superstructure. The first one is the seismic isolation effect that occurs due to the horizontal flexibility of slender RC columns; thus, the isolation effect increases the period of the structure and decreases the peak acceleration value of the top slab. The second one is the beneficial anti-resonance effect of the resonators of
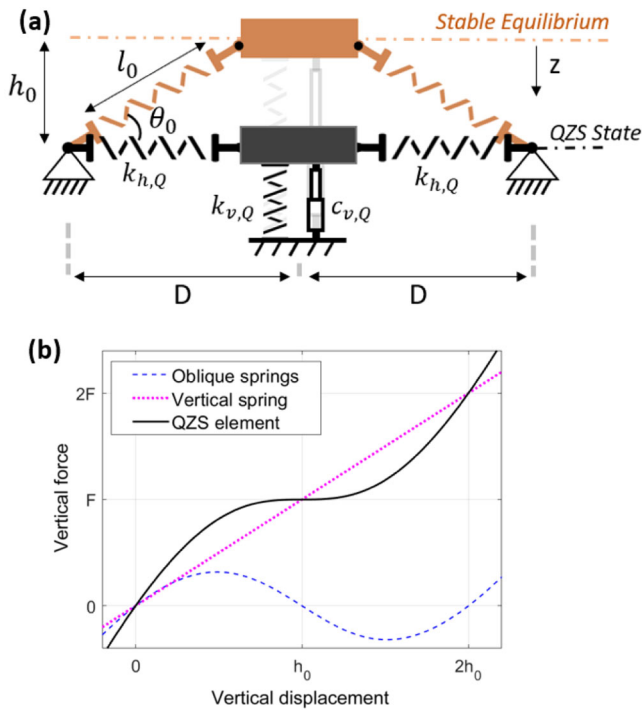
FIGURE 4 Quasi-zero stiffness (QZS) element: (a) mass-spring representation; (b) force-deformation relationships

the primary cells that act like huge tuned mass dampers (TMD) and damp out a significant amount of energy in both horizontal and vertical directions also with the contribution of physical damping. Similar to conventional TMDs, to obtain the most favorable performance of the resonators, they need to be optimized.

3.2 | The QZS unit cell

To increase the vertical flexibility of the metafoundation and explore the combined dynamics with linear cells, the QZS mechanism is introduced as an additional element. Accordingly, the improvements provided by these components are deemed to be investigated. While many ingenious configurations are possible to replicate the QZS mechanism, for simplicity, the simple mechanism depicted in Figure 4a is exploited. As a result, the two horizontal springs endowed with a stiffness $k_{h,Q}$, the so-called oblique springs, exert a negative stiffness effect.

In particular, the negative stiffness region entailed by the prestressed oblique springs in the horizontal configuration compensates for the positive stiffness of vertical springs. As a result, high static and low dynamic stiffness effects are achieved as illustrated in Figure 4b. To enrich dynamic effects, the aforementioned springs can exert a nonlinear behavior (Carrella et al., 2009); moreover, one can achieve a similar behavior by means of buckled beams or cam-

roller mechanisms (Huang et al., 2014; Liu et al., 2013; Zhou et al., 2015). The static vertical loads are taken by the vertical spring of stiffness $k_{v,Q}$ while damping is exerted through a damper with a coefficient $c_{v,Q}$. The aforementioned vertical springs and dampers are physically made with composite columns located at the cell boundaries.

Regarding Figure 4b, to achieve near-zero stiffness values, the stiffness parameters of oblique springs are deemed to be calibrated at the stability limit. Owing to the 3D characteristics of the unit cell, four oblique springs can be considered. Thus, the proposed formulation foresees the use of n_h oblique springs, and the formulations originally presented by Carrella et al. (2007) were revised to allocate more springs. The effect of horizontal displacement on the vertical force–deformation relationship was neglected due to the high horizontal stiffness of the columns. The proof is provided in Section 6.3. The potential energy $U(z)$ of the system can be expressed as

$$U(z) = n_h \cdot \frac{1}{2} k_{h,Q} [l(z) - l_0]^2 + \frac{1}{2} k_{v,Q} z^2$$

$$l(z) = \sqrt{(h_0 - z)^2 + D^2} \qquad (4)$$

where z defines the vertical displacement, and l_0 is the initial oblique spring length. By differentiation of $U(z)$, the force–deformation relationship $f_v(z)$ can be expressed as

$$U'(z) = f_v(z) = n_h k_{h,Q} (h_0 - z) \left(\frac{l_0}{l(z)} - 1 \right) + k_{v,Q} z \quad (5)$$

At the unstable static equilibrium, the bistable system exhibits a negative stiffness peak. One can linearize $f_v(z)$ around $z = h_0$ by means of Taylor's series expansion and obtain

$$f_v(z) = k_{v,Q} z + n_h k_{h,Q} \left(1 - \frac{l_0}{D} \right) (z - h_o) + O \left((z - h_o)^2 \right) \qquad (6)$$

For simplicity, the initial angle θ_0 at the stable equilibrium with $\cos(\theta_0) = D/l_0$ and the stiffness ratio $\alpha = k_{h,Q}/k_{v,Q}$ are defined and introduced in Equation (6) and Figure 4. Hence, through differentiation and assuming $z = h_0$, the stiffness K_Q at the unstable equilibrium can be expressed as

$$K_Q = \frac{df_v(h_0)}{dz} = k_{v,Q} \left(1 + n_h \alpha \left(\frac{\cos(\theta_0) - 1}{\cos(\theta_0)} \right) \right) \quad (7)$$

where $K_Q = 0$ entails the unique relationship between the aforementioned parameters,

$$\theta_0 = \cos^{-1} \left(\frac{n_h \alpha}{n_h \alpha + 1} \right) \qquad (8)$$
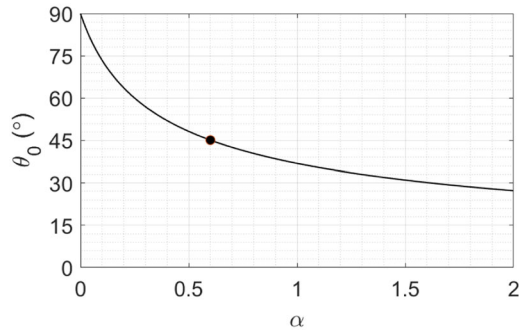
FIGURE 5 Relationship between the stiffness ratio α and the initial angle θ_0 that characterizes the QZS component
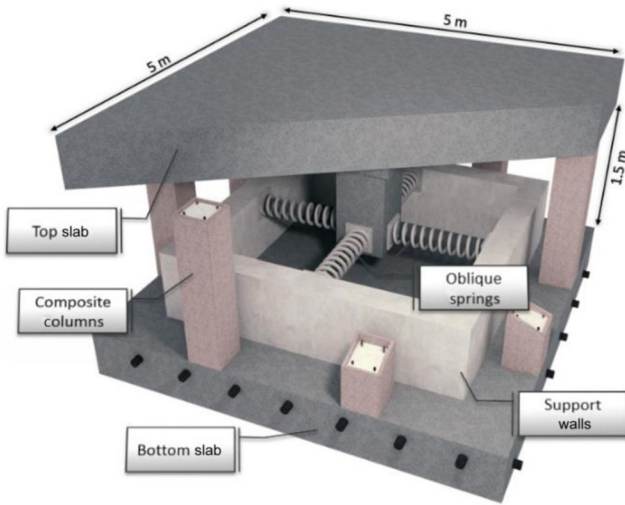

FIGURE 6 Schematics of the QZS unit cell and relevant components
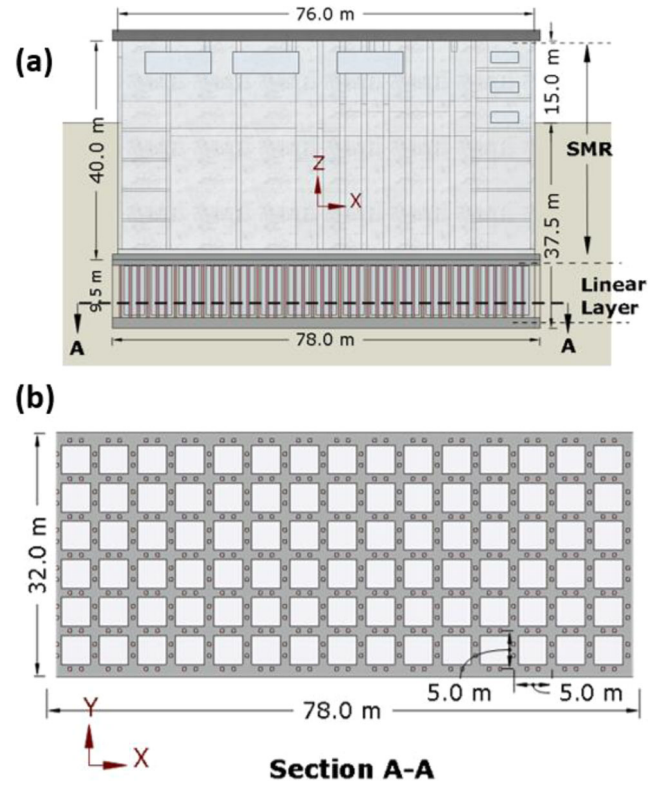

FIGURE 7 Linear metafoundation (LM) layout: (a) section view of coupled LM-SMR, (b) plan view of the linear layer

directions read,

$$f_{h,o}(x,z) = \frac{n_h k_{h,Q} D}{2\sqrt{z^2 + D^2}} x$$

$$f_{v,o}(z) = n_h k_{h,Q}(h_0 - z)\left(\frac{l_0}{l(z)} - 1\right) \qquad (9)$$

4 | MODELING AND SEISMIC DESIGN OF METAFOUNDATIONS

As anticipated, this research is centered on two types of metafoundations, LM and QM, which are based on the aforementioned cells. The coupled LM-SMR system in terms of size and layout is depicted in Figure 7. The QM entails single or multiple QZS layer(s) made of QZS cells; and both the location—with regard to a linear layer, top or bottom—and the number of these layers were investigated. To assess the performance of both the LM and QMs, accurate modeling is crucial, and the details of the modeling procedure are given in Section 4.1 with regard to the configuration QM-B1. The QM-B1 layout foresees a QZS layer located under the linear layer as shown in Figure 8.

Both metafoundations LM and QMs contain a single layer of linear unit cells. As mentioned above, due to the

which characterize the QZS behavior. The relationship between the stiffness ratio α and the initial angle θ_0 that characterizes the QZS element is depicted in Figure 5. As a result, in this study the chosen value $\theta_0 = 45°$ entails $\alpha = 0.6$.

To exert the QZS behavior at the proper value $\theta_0 = 45°$, it is assumed that the gravity loads are initially taken by the columns. When equilibrium is achieved, then the oblique springs are installed in a pre-compressed state as shown in Figure 6. Each QZS cell contains vertical columns, four oblique springs, the support walls for the oblique springs and a top slab with a rigid foot that extends to the center of the oblique springs. Like the lattice of linear cells, a total of 90 QZS cells was utilized for a QZS layer.

The horizontal reaction force produced by the oblique springs can be represented as a nonlinear function of both horizontal (x) and vertical (y) displacements. It can be easily derived by considering a small-angle approximation; thus, the reaction forces of the oblique springs in both
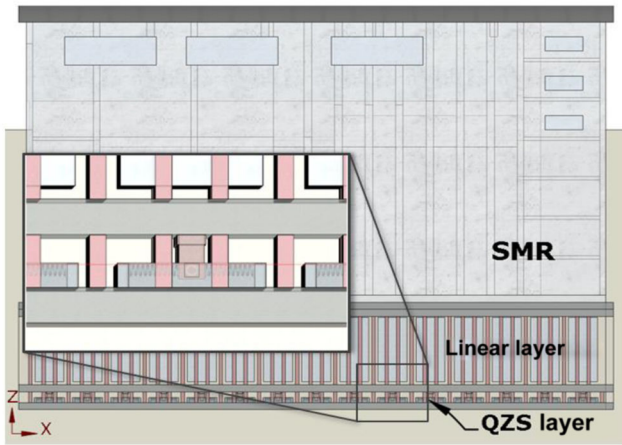
FIGURE 8 Section view of the QM-B1 solution and zoom of the QZS layer

isolation effect caused by column flexibility, the columns of these cells significantly affect the metafoundation performance. Hence, the height H and design section properties need to be carefully selected.

4.1 | Modeling of the metafoundations

The whole coupled metafoundation–SMR system was discretized in terms of springs, dashpots, and mass elements. Some relevant nodes that define geometrical entities used to connect these elements are shown in Figure 9; moreover, they are associated with kinematical quantities, that is, horizontal, vertical, and rotational DoFs. In fact, given the asymmetry of the superstructure and the moment related to the height of the SMR mass, see Section 2, the rocking motion has to be simulated. Accordingly, and in addition to horizontal and vertical DoFs, rotational DoFs are also introduced in each node.

The discretized QM-B1 model with SMR is sketched in Figure 9. The SMR block in the figure represents the 9 DoFs model defined in Figure 2, and the foundation slab was replaced with QM-B1. Due to horizontal, vertical, and rotational DoFs, it must be emphasized that each mass matrix $\mathbf{M}_{r,j}$ of a resonator is diagonal and 3×3; conversely and due to additional masses, see Figure 2, the $\mathbf{M}_{\mathbf{SMR}}$ of the SMR is diagonal and 9×9. The columns of the layers are modeled as elastic translational springs and dampers. Differently from the rotational spring used between the SMR and the foundation, resonator-slab, slab-slab, and slab-ground rotational couplings are yielded by translational springs only. Accordingly, the distance of each column, oblique and resonator springs to the center of gravity (C.G.) of the main slab, that is, d_c, d_o, and d_r governs the rotational stiffness of the relevant nodes. For simplicity, it was assumed that the soil was characterized

by small deformations, and therefore soil-structure interaction was neglected; however, soil characteristics are included both in soil filters, see Section 5.1, and recorded accelerograms, see Section 6.2.

In agreement with Figure 9, the diagonal mass matrix of the coupled system denoted with the subscript c reads,

$$\mathbf{M_c} = diag\left(\mathbf{M_{SMR}}, \mathbf{M_{m,L}}, \mathbf{M_r}, \mathbf{M_{m,Q}}\right) \quad (10)$$

where $\mathbf{M_{SMR}}$ is the mass matrix consisting of the masses defined in Figure 2. The $\mathbf{M_{m,L}} = diag(m_L, m_L, I_L)$ and $\mathbf{M_{m,Q}} = diag(m_Q, m_Q, I_Q)$ are 3×3 diagonal mass matrices for the main slab of the linear layer and QZS layer, respectively. Similarly, the stiffness matrix of the coupled system reads,

$$\mathbf{K_c} = \begin{bmatrix} \mathbf{K_{SMR}} & -\mathbf{K_s} & 0 & 0 \\ -\mathbf{K_s} & \mathbf{K_{m,L}} + \mathbf{K_s} + \mathbf{BK_{res}B^T} & -\mathbf{B} \cdot \mathbf{K_{res}} & -\mathbf{K_{m,L}} \\ 0 & -\mathbf{K_{res}B^T} & \mathbf{K_{res}} & 0 \\ 0 & -\mathbf{K_{m,L}} & 0 & \mathbf{K_{m,Q}} + \mathbf{K_{m,L}} \end{bmatrix} \quad (11)$$

where $\mathbf{K_{SMR}}$ defines the stiffness matrix computed with respect to the spring arrangement in Figure 2. $\mathbf{K_S}$ was defined in Equation (1), and the matrices $\mathbf{K_{m,L}}$ and $\mathbf{K_{m,Q}}$ include the stiffness terms relevant to the columns of the corresponding layer. More precisely, $\mathbf{K_{m,L}}$ reads,

$$\mathbf{K_{m,L}} = diag\left(\sum \mathbf{k_{h,L}}, \sum \mathbf{k_{v,L}}, \sum \mathbf{k_{v,L}d_c}\right) \quad (12)$$

The $\mathbf{K_{m,Q}}$ can be computed similarly. As expected, the rocking effect is of particular interest, and it was deepened in Section 6. From Figure 7b, one can argue that 15 resonators can be utilized along the X direction and six along the Y direction. Particularly in the X direction, each resonator was associated with a node with a mass matrix $M_{r,j}$, where the subscript j depicts the jth resonator from the left-hand side of Figure 9. To reduce the computational expense, the Y direction was excluded by the analysis and, because cells are identical, the six resonators out of the plane were dynamically condensed by simply summing masses and stiffness terms. Thus, the resonator matrices $\mathbf{M_{res}} = diag(M_{r,1}, \ldots, M_{r,j})$ and $\mathbf{K_{res}} = diag(K_{r,1}, \ldots, K_{r,j})$ define $j \times j$ diagonal matrices where $\mathbf{M_{r,j}}$ and $\mathbf{K_{r,j}}$ represent the stiffness and mass matrices of a single condensed resonator,

$$\mathbf{M_{r,j}} = \begin{bmatrix} m_r & 0 & 0 \\ 0 & m_r & 0 \\ 0 & 0 & I_r \end{bmatrix} \mathbf{K_{r,j}} = \begin{bmatrix} k_{h,r} & 0 & 0 \\ 0 & 2k_{v,r} & 0 \\ 0 & 0 & k_{v,r}(d_{r,2j-1} - d_{r,2j}) \end{bmatrix} \quad (13)$$

More precisely, each term m_r, I_r, $k_{h,r}$, and $k_{v,r}$ results from the summation of six resonators and associated springs in the out-of-plane direction. The damping
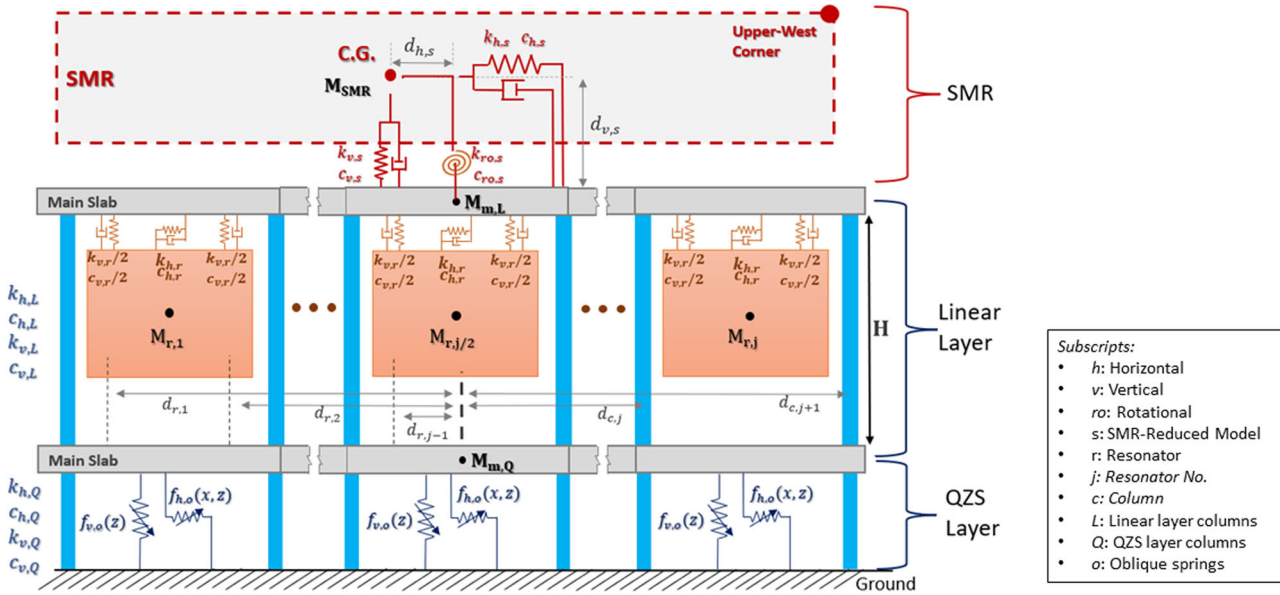
FIGURE 9 Coupled QM-B1 and SMR spring-mass model. C.G. defines the center of gravity of the SMR

matrices can be assembled in a similar fashion. As a result, the system of equations of motions (EoMs) can be expressed in the Euler–Lagrange form:

$$\mathbf{M_c}\ddot{\mathbf{u}}(t) + \mathbf{C_c}\dot{\mathbf{u}}(t) + \mathbf{K_c}\mathbf{u}(t) + \mathbf{F_o}(\mathbf{u}(t)) = \mathbf{F_{ext}}(t) \quad (14)$$

where $\mathbf{F_o}$ is the nonlinear force function of the oblique springs that gathers the relationships stated in Equation (9) in agreement with the QM-B1 configuration. The aforementioned modeling approach was utilized for the remaining configurations investigated. The entailed discretized coupled models were adopted for design, optimization, and analysis purposes.

4.2 | Design of the LM

To maximize the efficiency of the LM, one needs to achieve the maximum antiresonance phenomenon and, therefore, maximize the mass of the resonators; so the volume of each resonator occupies the maximum space available in the unit cell. Obviously, the maximum total displacement demand of the resonators, that is, 0.5 m, was taken into account. The efficacy of this solution can be appreciated in Basone et al. (2019).

Given the fire standards associated with NPPs, composite columns were employed in the cells as depicted in both Figures 3 and 6. Owing to the low shear stiffness and high moment/axial capacity required, hollow square steel sections filled with RC were considered in accordance with Eurocode 1994-1-2(2005a). In particular, a 6% steel reinforcement ratio and a concrete grade C50/60 was

considered and the target fire-resisting rating of R180 was selected. In view of feasibility, the aforementioned design also complies with the Eurocodes 1993-1-1(2005b) and Eurocodes 1994-1-1(2004a).

All parts of the LM were conceived to satisfy the SSE limit state that is related to a lower probability of earthquake exceedance under which relevant important components and structures must be designed to allow for a safe shutdown without damage (ASCE/SEI, 2016). Therefore, the behavior-reduction factor is taken as $q = 1$ under the horizontal $PGA_H = 0.3$ g. The corresponding design vertical acceleration is also considered with $PGA_v = 2/3 * PGA_H$. The design spectra defined by Eurocode 1998-1(2004b) were utilized for both horizontal and vertical directions. Again, in accordance with the European seismic standard, the excitation in the orthogonal planar directions X or Z was reduced to 30% interchangeably. The design was carried out with the inclusion of several modes up to 85% of modal masses and responses were combined with a complete quadratic combination (Chopra, 2017).

Due to the initially unknown stiffness and damping parameters of the resonators, the design phase was conducted iteratively. The design of the columns, indeed, is significantly affected by the stiffness of the resonators. Nonetheless, their stiffness was part of an optimization problem that depend on the column parameters. Accordingly, the initial design of the columns was conducted with guessed parameters of the resonators, and subsequently the optimization of the resonator parameters was carried out. Then, the column design was performed with the optimized resonator parameters, until a satisfactory design was achieved.

4.3 | Optimum column height selection for the LM

Based on frequency and time domain analyses, Basone et al. (2019) clearly showed that the performance of an LM under the horizontal component of an earthquake strongly depends on the horizontal stiffness of the main—exterior–cells, that is, the columns. In this sense, the higher the height of the columns, the better the vibration mitigation performance of the finite lattice due to the lower horizontal stiffness of columns. Clearly, this favorable effect may not be linearly scaled due to design, mainly strength limitations. Other limiting factors are represented by the metafoundation size that cannot be scaled down with regard to costs and workmanship. It is apparent that the height of the LM is strongly limited by both cost and space below the superstructure. As the height increases, indeed, both material and excavation costs rapidly increase while soil layer properties might limit depth. To simulate the aforementioned limitations, both construction costs and the LM performance expressed by means of horizontal stiffness values are considered together.

More precisely, these two objective functions constitute a bicriteria optimization problem where when stiffness values reduce,-with a subsequent performance increase, the cost increases in a nonlinear fashion. Moreover, given the column height H, see Figure 3, multiple column designs with regard to design standards are possible, and the most flexible column does not guarantee the lowest cost due to the increased mass of resonators. As a result, the selection of H requires the solution of a Pareto front optimization problem where no better solution exists for both flexibility and cost. To quantify the LM horizontal stiffness, the period ratio ε is defined as

$$\varepsilon = \frac{T_s^2}{T_{LM}^2} = \left(2\pi\sqrt{\frac{m_s}{k_{h,s}}}\right)^2 \Big/ \left(2\pi\sqrt{\frac{m_s + m_L}{k_{h,L}}}\right)^2 \quad (15)$$

where T_{LM} and T_s correspond to the period of the coupled system with an LM and the period of the system with a rigid foundation, respectively. In agreement with seismic isolation theory (Kelly, 1990), if $\varepsilon \leq 1\%$, the design of the isolation system can be considered effective. On the other hand, the approximate costs of LMs were determined with the available price information of southern European countries taking into account excavation, steel, concrete, and workmanship costs. To simplify the calculations, the fixed metafoundation costs were not included. The fixed costs correspond to the cost of the material or work items that are subject to no change as the height changes, such as the cost of the ground slab and main slab. The details of cost approximations are given in the Appendix. Along the
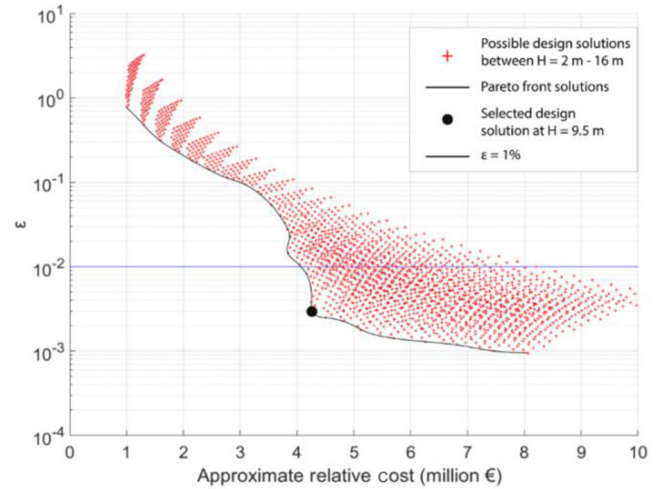

FIGURE 10 Design solutions for different LM heights and selected solution
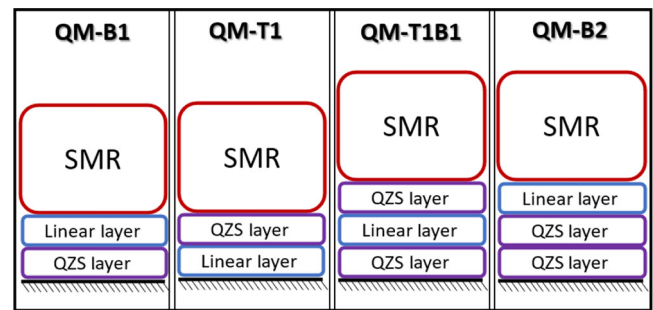

FIGURE 11 Metafoundations with QZS layer (QM) configurations (with abbreviations on top)

line of multi-objective optimization, multiple LMs with heights, 2 m ≤ H ≤ 16 m were designed, and all solutions together with the Pareto frontier are presented in Figure 10. Due to the low approximate relative cost and stiffness, a design corresponding to H = 9.5 m was selected. The entailing cross-section dimensions of the encased columns read 440 mm in width and 10 mm in thickness. The horizontal period T_m of the LM reads 2.3 s and entails $\varepsilon_m = 0.30\%$ and the relative cost of about 4.28 million euros.

4.4 | Design of the QZS layers

The location of the QZS layer(s) with regard to the linear layer, and the number of these layers can significantly affect the metafoundation performance. Accordingly, four different QM configurations were designed and analyzed. For simplicity, both configurations and nomenclature are depicted in Figure 11. The design of the QZS layer columns was also conducted similarly to what was done in Section 4.2. As anticipated, the vertical columns of the

TABLE 2 Column properties for the metafoundations with quasi-zero stiffness (QZS) layers (QM) configurations

	Linear layer columns		QZS layer columns	
	Width (mm)	Thickness (mm)	Width (mm)	Thickness (mm)
QM-B1	440	10	340	10
QM-T1	460	10	380	14
QM-T1B1	480	10	400	16
QM-B2	460	10	340	12

QZS layer were modeled as positive stiffness springs and dampers aligned to the columns of the linear layers.

Based on the Pareto front solution of the previous subsection, the height of the linear layer in each configuration was taken constant as H = 9.5 m. Since the introduction of the QZS layer influences the design of the linear layer, it was redesigned accordingly. The finalized cross-sectional properties of the columns for each QM configuration are gathered in Table 2.

5 | OPTIMIZATION OF RESONATOR PARAMETERS

In order to obtain maximum performance from the proposed LM and QMs, the resonator parameters, given in Equation (3), need to be optimized regarding stochastic seismic excitations. Since the mass of the resonators are constant, the parameters for the optimization problem simplify to $\omega_{h,r}$, $\zeta_{h,r}$, $\omega_{v,r}$ and $\zeta_{v,r}$.

5.1 | Optimization problem

In view of computational savings and linear relationships involved, the optimization was performed in the frequency domain. Accordingly, the system of EoMs (14), subjected to the Fourier transform reads,

$$-\omega^2 \mathbf{M_c u}(\omega) + i\omega \mathbf{C_c u}(\omega) + \mathbf{K_c u}(\omega) = -\tau \mathbf{M_c \ddot{u}_g}(\omega) \quad (16)$$

where ω defines the circular input frequency and $\mathbf{F_{ext}}(t) = -\tau \mathbf{M_c \ddot{u}_g}(t)$. For the QM configurations, the linearization of the force function $\mathbf{F_o}$ was required. Hence $\mathbf{F_o}$ relevant to the oblique springs was linearized around $z = h_0$ and $x = 0$, as in Equation (6), and comprised in $\mathbf{K_C}$. The corresponding displacement transfer function reads,

$$\mathbf{H_d}(\omega) = (-\tau \mathbf{M_c}) \cdot \left(-\omega^2 \mathbf{M_c} + i\omega \mathbf{C_c} + \mathbf{K_c} \right)^{-1} \quad (17)$$

Taking the derivative of Equation (17), one gets,

$$\mathbf{H_{a,rel}}(\omega) = -\omega^2 \mathbf{H_d}(\omega) \quad (18)$$

where $\mathbf{H_{a,rel}}$ is the relative acceleration transfer function; thus, the absolute acceleration transfer function reads: $\mathbf{H_{a,abs}}(\omega) = \tau - \mathbf{H_{a,rel}}(\omega)$. Consequently, the PSD of the system regarding the i-th DoF can be obtained as

$$\mathbf{S_Q}(\omega) = \left| \mathbf{H_{a,abs}}(\omega) \right|^2 \cdot \mathbf{S_{\ddot{u}_g}}(\omega) \quad (19)$$

where $S_{\ddot{u}_g}$ is the power spectral density (PSD) of the external force, $\mathbf{F_{ext}}(t)$ due to seismic acceleration. In particular, the PSD function was used to simulate both soil properties and the stochastic nature of the earthquakes. Accordingly, the seismic input was assumed to be a weakly stationary Gaussian filtered white noise with zero mean and spectral intensity S_0.

To set the input for both horizontal and vertical directions, S_0 is filtered with both the Kanai–Tajimi (KT) (Kanai, 1957) and the filter proposed by Clough and Penzien (CP) (2003). While the first filter takes the soil characteristics into account, the second one filters the low-frequency range to avoid unrealistic high values near the null frequency. For brevity, the modulus of the combined filter is referred to as the KTCP filter and reads,

$$S_{\ddot{u}_g}(\omega) = S_0 \cdot \frac{4\zeta_g^2 \omega_g^2 \omega^2 + \omega_g^4}{4\zeta_g^2 \omega_g^2 \omega^2 + \left(\omega_g^2 - \omega^2 \right)^2}$$
$$\cdot \frac{\omega^4}{4\zeta_f^2 \omega_f^2 \omega^2 + \left(\omega_f^2 - \omega^2 \right)^2} \quad (20)$$

In the horizontal direction, the parameters of the filter are chosen to meet the seismic characteristics of Priolo Gargallo, at a return period of 2475 years, that is, the SSE. Their values read $S_0 = 0.09$ m^2/s^3, $\omega_g = 14$ rad/s, $\zeta_g = 0.6$, $\omega_f = 0.75$ rad/s and $\zeta_f = 1.9$. The details of the calculation of these values can be found in Basone et al. (2019). The CP filter parameters assume the same values in the vertical direction, while the KT parameters are scaled in agreement with the data provided in Kramer (1996). Correspondingly, the soil frequency is scaled with 1.3, that is, $\omega_g = 18.2$ rad/s while the high damping ratio ζ_g was kept constant. So, the variance of the absolute acceleration σ_{acc} is computed using the Wiener–Khintchine

relationship as

$$\sigma_{acc}^2 = \int\limits_0^{+\infty} \mathbf{S_{Q,i}}(\omega) \cdot d\omega \qquad (21)$$

To nondimensionalize the computed variances, the performance indices (PI) were introduced. One can define,

$$PI_{Hor} = \frac{\sigma_{Hor}}{\sigma_{Hor,RF}} PI_{Ver} = \frac{\sigma_{Ver}}{\sigma_{Ver,RF}} \qquad (22)$$

where the subscript RF indicates the RF case. Therefore, the multi-objective optimization problem was defined as

$$\mathbf{Z} = \left\{ \omega_{h,r}, \zeta_{h,r}, \omega_{v,r}, \zeta_{v,r} \right\}$$
$$\min\left(PI_{Horz}(\mathbf{Z})\right) \text{ and } \min\left(PI_{Vert}(\mathbf{Z})\right) \qquad (23)$$

For the optimization, the tolerance values were selected as 0.1 rad/s for frequencies and 1% for damping. The search space for the optimization problem was limited to

$$1\text{rad/s} < \omega_{h,r} < 30\text{rad/s} \quad 0.05 < \zeta_{h,r} < 0.40$$
$$20\text{rad/s} < \omega_{v,r} < 100\text{rad/s} \quad 0.05 < \zeta_{v,r} < 0.40 \qquad (24)$$

5.2 | Requirements for optimization of metafoundations

The optimization problem at hand can be solved using various methods and strategies. Given the variety of design parameters of both the LM and QMs, the selected optimization strategy must satisfy the requirements resulting from complex metafoundation configurations. Thus, the aforementioned requirements can be summarized herein.

1. The optimization problem is nonlinear, and differentiation is complicated. The method should accept boundaries for the parameters. Moreover, if the user chooses to divide the resonators into subgroups with different parameters or multiple layers with different properties, see Bursi et al. (2021), the number of optimization parameters may rapidly increase. Likewise, the user can also target more than one node or DoF of the superstructure to be optimized; more so, the method should be futureproofed for possible optimization problems.
2. Algorithms that require an initial guess of the solution set are unfeasible, as initial estimates may be located in an isolated region where no improvement of the function value can be achieved. Accordingly, a robust optimization method should not require an initial guess of the solution set.

3. The metafoundation–SMR system exhibits significant coupling between horizontal and vertical DoFs due to the rotational modes as explained in Section 4.1. Thus, the optimization has to consider the performance in both horizontal and vertical directions simultaneously, which renders the optimization problem multi-objective. To simplify, the WSM can be used to synthesize a single objective function. However, the selection of the weight ratios is controversial and needs some care.
4. The parameters of the optimization problem do not require to be tuned precisely. This is an important aspect because most optimization algorithms are designed to work with significant precision; however, in this specific case, the realization of the resonator frequency or damping value to a certain computed precision is not easy and probably not needed. Moreover, high precision stiffness and damping values may not be yielded at the construction stage.
5. The sensitivity of the performance of the metafoundation to the optimization parameters needs to be quantified, and the computation of sensitivity matrices between parameters and objective functions is beneficial to the designer.

With regard to the first three points and considering the WSM with equal weights, only a handful of algorithms is available. One well-suited deterministic method is the n-dimensional extension of the GSS (n-GSS) algorithm (Chang, 2009); it is a simple method if the problem is represented by a single objective. However, it may converge into a local minimum, and the curse of dimensionality issue appears as the number of parameters increases. From heuristic algorithms; the GA, PSO, and SA, among others, are well-known methods that can satisfy the requirements. The disadvantages of these algorithms are that they generally require many function evaluations with restarts, and they may exhibit inaccuracy and inconsistency due to the nature of the stochastic search; see, in this respect, Section 5.4. Moreover, none of these methods yields any information about the global sensitivity of the problem and does not consider multi-objectivity.

In sum, the combination of the disadvantages of the aforementioned optimization methods together with the lack of some requirements necessitates the development of a specialized optimization procedure. Consequently, a simple but efficient optimization procedure is suggested hereinafter. The proposed procedure focuses not only on finding the optimal solution but also provides global sensitivity information about parameters and objectives. It is explained herein.

5.3 | A new optimization procedure

Both configurations and user-dependent choices entail the optimization problem of a metafoundation characterized by different optimization parameters and objective functions. In several cases, however, each objective function is sensitive to a few parameters and even fewer of them interact with each other. As a result, the optimization problem can be separated into multiple suboptimization problems where each parameter is optimized together with the interacted parameters. Moreover, the sensitivity of objective functions to each parameter can be used as weight for the WSM method. Accordingly, each parameter can be optimized by targeting the most sensitive objective function. In this respect, the first step of the procedure starts with the execution of a global sensitivity analysis and then uses the sensitivity information to group the parameters to be optimized separately with restect to the impact on the objective functions. For brevity, the first part of the procedure is named sensitivity-based parameter grouping (SPG) strategy.

To obtain global sensitivity information of the problem on hand, Sobol's sensitivity indices (Sobol, 1993) and the total variance of the objective functions are considered. Both the evaluation of Sobol's indices and the consequent parameter grouping are explained herein. Let us assume the model $Y_k = f_k (X_1, X_2, \dots, X_{n_i})$ with n_{in} independent and uniformly distributed input parameters, for kth function of n_{obj} objective functions. Both the first and the second order Sobol's indices can be obtained by a variance decomposition,

$$S_k(i,i) = \frac{V_i}{V_k} = \frac{V_{X_i}\left[E_{X_{\sim i}}(Y_k|X_i)\right]}{V[Y_k]} \quad S_k(i,j) = \frac{V_{ij}}{V_k} \quad (25)$$

where X_i is the ith (or jth) parameter, and $X_{\sim i}$ denotes the set of all parameters besides X_i. Here, S_k represents the 2D sensitivity matrix of the kth objective function; hence, the third and higher-order interactions were not considered. By means of the second-order Sobol's indices $S_k(i,j)$, the interaction between parameters can be determined. Thus, when a parameter is started to be optimized, a limited interaction entails those irrelevant parameters are assumed to be constant and input parameters are reduced. Numerically, the threshold for the interaction was taken as 5% herein. Subsequently, if the interaction between two parameters is more than the threshold for each objective function, that is, $S_k(i,j) > 0.05$, the jth parameter should also be involved in the optimization of the ith parameter.

To compute Sobol's indices, the Monte Carlo sampling method was employed, and variances were computed through the estimator proposed by Janon et al. (2014).

$$S_v = \frac{\frac{1}{M}\sum_{m=1}^{M} Y_m \cdot Y'_m - \left(\frac{1}{M}\sum_{m=1}^{M}\left[\frac{Y_m + Y'_m}{2}\right]\right)^2}{\frac{1}{M}\sum_{m=1}^{M}\left[\frac{Y_m^2 + (Y'_m)^2}{2}\right] - \left(\frac{1}{M}\sum_{m=1}^{M}\left[\frac{Y_m + Y'_m}{2}\right]\right)^2} \quad (26)$$

where M is the total number of samples. In particular, the input vector can be separated into two parts as $Y = f(V, W)$ and S_v. The W' denote an independent copy W and; similarly, $Y' = f(V, W')$. S_v can be computed by simply inserting $V = \{X_i\}$. The second-order indices $S_k(i,j)$ are computed by subtracting the first-order indices of each parameter from the total effect of the two parameters, that is,

$$S_k(i,j) = S_{k[i,j]} - S_k(i,i) - S_k(j,j) \quad (27)$$

The multiple objective functions were rationally combined using the sensitivity data as weights of the WSM. Accordingly, $S_k(i,i)$ and the total variance $V[Y_k]$ were used to combine objective functions in terms of the effect of the ith parameter on the kth objective function. Therefore, for each parameter, the objective functions were combined as

$$Y_i^* = \sum_{k=1}^{n_{obj}} w_{i,k} \cdot Y_k \quad (28)$$

where $w_{i,k}$ is the weight factor and it can be computed as

$$w_{i,k} = S_k(i,i) \cdot V(Y_k) / \sum_{k=1}^{n_{obj}} S_k(i,i) \cdot V(Y_k) \quad (29)$$

Following the grouping of the parameters and the WSM, each suboptimization problem can be solved. From the aforementioned algorithms, the heuristic ones require a higher number of function evaluations in comparison to deterministic optimization schemes; and the only available deterministic algorithm n-GSS may fall into a local optimum. Therefore, the n-GSS algorithm was further modified and combined with the well-known grid search strategy, which is commonly used for hyperparameter optimization, and a hybrid multivariable deterministic recursive optimization algorithm was conceived. For brevity, the proposed algorithm is called grid section search algorithm (GrSS) and is briefly explained, herein.

Like the GSS algorithm, the GrSS uses the boundaries, $\{X_{i,\max}, X_{i,\min}\}$, for n_{in} parameters and defines the search space. Then, a grid of trial points was generated in an analogous way to the grid search strategy. For each dimension of the search space, n_g number of points are generated between the boundaries. Accordingly, n_g defines the user input. After each grid point is evaluated, the predefined region around the optimum point is preserved and the

search space is reduced to the new preserved region for subsequent iterations similar to the GSS method. The equidistance of the preserved region corners to the optimum point is computed as $(X_{i,\max} - X_{i,\min})/(2n_g - 2)$. The described steps define one iteration of GrSS; thus, the steps are repeated recursively until the distance in every dimension between the boundaries becomes smaller than the tolerance. For convenience and to reduce errors, after all suboptimization problems are solved, each parameter is re-optimized alone considering other parameters fixed with obtained optimum values. Consequently, the effect of the solution order of suboptimization problems is minimized.

It should be emphasized that the grid search strategy is based on an exhaustive search for the optimum; however, the given SPG strategy readily reduces the dimensionality and gives to GrSS a minimal number of parameters. Accordingly, despite the GrSS algorithm—alone—suffers from the curse of dimensionality, and the implementation of the SPG mitigates this issue beforehand and these algorithms are presented as one optimization procedure for metafoundations.

For brevity, the steps of the proposed optimization procedure are summarized herein:

1	**Input** optimization function: $[Y_1, \ldots, Y_{n_{obj}}] = f(X_1, \ldots, X_{n_{in}})$.
2	**Input** boundaries for each variable, $\{X_{i,\max}, X_{i,\min}\}$,
3	**Run** SPG (Sensitivity based Parameter Grouping) strategy
4	Generate sample points using Latin Hypercube Sampling
5	**Evaluate** f at sample points.
6	**Compute** $\mathbf{S}_k$ using Equations 26 and 27
7	Group parameters together with $\mathbf{S}_k(i,j) > 0.05$
8	Create suboptimization problems
9	**For** each suboptimization problem
10	**Compute**, Y^* using WSM (Equations 28 and 29)
11	**Run** GrSS
12	Divide search space into a grid with n_g point in each dim.
13	Evaluate the grid points
14	**Find** the point with minimum Y^*.
15	Preserve the region around the point with a distance equal to $(X_{i,\max} - X_{i,\min})/(2n_g - 2)$. and redefine the $\{X_{i,\max}, X_{i,\min}\}$
16	**If** the distance between the boundaries is less than tolerance
17	**Return** Line 8
18	**Else**
19	**Return** Line 10
20	**End if**
21	**End For** if all suboptimization problems solved
23	**Compute** $\mathbf{S}_k$ with all points evaluated in the procedure.
24	**Output** Optimized resonator parameters and sensitivity matrices

5.4 | Comparison of proposed optimization procedure

To verify the efficiency of the proposed optimization procedure, each LM and QM configuration was modeled and designed with layer heights H = 6, 8, 10, and 12 m. Accordingly, a total of 20 metafoundations—four different heights and five configurations—were considered. The metafoundations were optimized using n-GSS, GA, SA, PSO, and the SPG-GrSS procedures. For the SPG step, 100 sample points were generated and for GrSS, $n_g = 7$ was taken. For each method, the average function evaluations and the average relative error are presented in Tables 3 and 4, respectively. Herein, average corresponds to the average of the results for the four different H values. The given function evaluations include the evaluated functions in the SPG step, and the relative error was computed with regard to the results of a method characterized by the best result.

It can be concluded that the nondeterministic methods suffer from a high number of function evaluations while both GA and PSO exhibited the best performance. The overall performance of SA fell behind both GA and PSO. In terms of evaluated functions, the n-GSS achieved the best performance, but it exhibited the maximum error due to its tendency to fall in local minima. In sum, the proposed optimization procedure performed quite well. Considering the function evaluation difference between nondeterministic methods and the proposed procedure, the slight increase in the error is negligible. Despite a slightly increased number of function evaluations with regard to n-GSS, the proposed optimization procedure achieved significantly better results.

5.5 | Optimization results

The resonator parameters of LM and QMs with H = 9.5, see Section 4.3, were then optimized with the procedure proposed in Section 5.3. Relevant results are listed in Table 5. The lower PI values show that the QM improves its performance depending on the location and amount. The most favorable metafoundation for both horizontal and vertical performance is obtained with the QM-B2 case. Moreover, it appears that the position of the single QZS layer at the bottom of the metafoundation improves the performance greatly, differently from a placement at the top. In this last case, the flexibility effect entailed by the QZS layer is localized (Chandrashaker et al., 2016) and unfavorable. Similarly, the QM-T1B1 case performed worse than the case QM-B2.

The sensitivity matrices obtained from the proposed optimization procedure are also presented in Table 6 for LM and QM-B1 configurations. It can be observed that the vertical stiffness of the resonators influences and slightly couples the horizontal stiffness in PI_{Hor}; conversely, the horizontal stiffness of resonators is irrelevant for PI_{Ver}. In addition, the utilization of QZS layers significantly reduces the total variance of PIs: This corresponds to a minor sensitivity to resonator parameters.

TABLE 3 Average function evaluations for H = {6, 8, 10, 12 m}

	Genetic algorithm (GA)	Particle swarm optimization (PSO)	Simulated annealing (SA)	n-Dimensional extension of the golden section search (n-GSS)	Sensitivity-based parameter grouping (SPG)-GrSS
LM	2941	1680	3313	240	334
QM-B1	2836	1420	2648	240	336
QM-T1	3910	1450	3354	240	339
QM-T1B1	2048	1170	4356	240	319
QM-B2	2646	1340	2664	240	312

TABLE 4 Average relative error for H = {6, 8, 10, 12 m}

	GA	PSO	SA	n-GSS	SPG-GrSS
LM	0.04	0.00	2.40	17.58	0.26
QM-B1	0.09	0.08	2.39	1.81	0.51
QM-T1	0.16	0.14	3.72	2.25	0.85
QM-T1B1	0.23	0.22	0.44	1.23	1.00
QM-B2	0.15	0.14	1.80	1.32	0.53

TABLE 5 Optimization results for the resonator parameters of LM and QMs with H = 9.5 m

H = 9.5 m	$\omega_{h,r}$	$\zeta_{h,r}$	$\omega_{v,r}$	$\zeta_{v,r}$	PI_{Hor}	PI_{Ver}
LM	3.0	0.28	42.0	0.18	0.0525	0.7963
QM - B1	2.7	0.33	23.2	0.18	0.0397	0.2161
QM - T1	3.1	0.37	21.5	0.07	0.0537	0.2986
QM - T1B1	3.5	0.32	21.0	0.06	0.0503	0.1833
QM - B2	2.8	0.34	23.6	0.16	0.0333	0.1331

tively. For computational convenience, that is, the use of the explicit fourth-order Runge–Kutta method, the system of EoMs (14) is expressed in state-space:

$$\begin{bmatrix} \dot{\mathbf{x}}_1 \\ \dot{\mathbf{x}}_2 \end{bmatrix} = \begin{bmatrix} \mathbf{x}_2 \\ -\mathbf{M}_C^{-1}(\mathbf{K}_C\mathbf{x}_1 + \mathbf{D}_C\mathbf{x}_2 + \mathbf{F}_0(\mathbf{x}_1)) + \mathbf{F}_{ext}(t) \end{bmatrix} \quad (30)$$

where $\mathbf{x}_1 = \mathbf{u}(t)$.

In view of a thorough comparison, the proposed LM and QM configurations were compared with the SMR model endowed with an RF and a standard isolated solution with friction pendulum devices (FPDs). The FPD isolators are selected from the market (FIPMEC, 2022); and a proper design entails a total of 90 FIP-DM 3050/500(3100) isolators. The effective fundamental period of the coupled system with the SMR is computed as $T_{FPD} = 2.57$ s, which corresponds to $\varepsilon_{FPD} = 0.24$ % by Equation (15). To take into account the vertical stiffness of each isolator, a 2-mm deflection under the design axial load was assumed.

6 | RESPONSES OF THE COUPLED SYSTEMS

To assess the performance of the proposed metafoundations, nonlinear frequency and THA were performed using harmonic input and a set of accelerograms, respec-

6.1 | Responses in the frequency domain

The aforementioned metafoundations were conceived with two main characteristics: (i) the introduction of isolation flexibility to attenuate seismic displacements/

TABLE 6 Computed Sobol's indices and total variances of LM and QM-B1

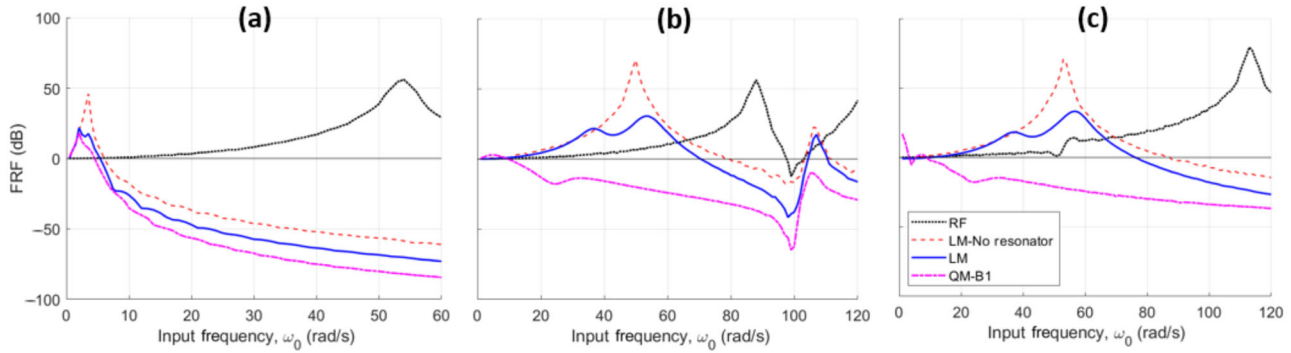| Sobol's indices		PI_{Hor}				PI_{Ver}			
H = 9.5 m		$\omega_{h,r}$	$\zeta_{h,r}$	$\omega_{v,r}$	$\zeta_{v,r}$	$\omega_{h,r}$	$\zeta_{h,r}$	$\omega_{v,r}$	$\zeta_{v,r}$
LM	$\omega_{h,r}$	0.852	0.009	0.042	0	0	0	0	0
	$\zeta_{h,r}$	–	0.006	0	0	–	0	0	0
	$\omega_{v,r}$	–	–	0.088	0	–	–	0.927	0.012
	$\zeta_{v,r}$	–	–	–	0	–	–	–	0.060
	$V(Y_k)$	1.86E-02				1.16E+00			
QM-B1	$\omega_{h,r}$	0.958	0.029	0.006	0.004	0	0	0.00	0.00
	$\zeta_{h,r}$	–	0	0	0	–	0	0.00	0.00
	$\omega_{v,r}$	–	–	0	0	–	–	0.987	0.006
	$\zeta_{v,r}$	–	–	–	0.002	–	–	–	0.006
	$V(Y_k)$	6.26E-04				4.14E-05			

FIGURE 12 Frequency response functions (FRF) with regard to: (a) horizontal, (b) vertical, and (c) rotational directions

accelerations; (ii) the adoption of the anti-resonance effect of resonators to mitigate seismic waves in both horizontal and vertical directions. Moreover, the utilization of multiple cells along the X and Y axis results in the prevention of rocking responses. In addition, the presence of the QZS layers introduces a fourth benefit, additional flexibility into the vertical component of the system. To discriminate between isolation and attenuation characteristics, four coupled cases are considered: (i) the RF; (ii) the LM without resonators; (iii) the LM, and (iv) the QM-B1. In the second case, the resonators of the linear unit cells were removed to highlight the effect of resonators.

Each case was excited by means of a time-harmonic displacement/rotation - $A_0 \sin(\omega t)$—applied from the ground ($\mathbf{F_{ext}} = 0$). Each peak response A was read from the SMR C.G. node. Hence, the frequency response function (FRF) for each case was evaluated as

$$FRF = 20 \cdot \log_{10}(A/A_0) \tag{31}$$

The FRFs were obtained for horizontal, vertical, and rotational DoFs and are presented in Figure 12. A reader can observe that, compared to the RF case, the introduced flexibility reduces resonant peak frequencies in all directions. Conversely, the absence of resonators entails amplitude peaks with significant magnitude. Finally, resonators with the QZS layer significantly reduce the vertical component responses in the high-frequency range.

6.2 | Seismic input

A set of eight recorded accelerograms with a 2% probability of exceedance in 50 years, that is, relevant to the SSE, were employed to evaluate the performance of the coupled systems. Thus, the selection of the accelerograms for both horizontal and vertical components follows the principle sketched in Figure 13; more precisely, both the mean spectrum and the mean spectrum plus one standard

deviation of the selected accelerograms match with the uniform hazard spectrum (UHS) of Priolo Gargallo, Sicily, Italy, in a least-square sense. Accordingly, let us consider s_0 be the target spectrum value vector, that is, the UHS; and evaluate $\mathbf{S}$, that is, the spectra matrix of the n_a accelerograms. One can define a vector of n_a selection coefficients, $\boldsymbol{\alpha}$, where each element can only take a binary value of 1 or 0, and the sum of the elements is equal to n_s, that is, number of accelerograms to be selected. Therefore, the following optimization problem can be solved for $\boldsymbol{\alpha}$:

$$\min\left(\left\| \frac{\mathbf{S}\boldsymbol{\alpha}}{n_s} - \mathbf{s_0} \right\|^2 \right) \tag{32}$$

The selection is performed with all possible combinations of the n_s accelerograms among a set of n_a records, and the dispersion of the records about the mean spectrum is taken into account. The details of the selected accelerograms are provided in Table 7. Successively, nonlinear THA were conducted using the set of selected accelerograms. The relevant external force used in Equation (30) reads $\mathbf{F_{ext}}(t) = -\tau \mathbf{M_c} \ddot{\mathbf{u}}_\mathbf{g}(t)$.

6.3 | Acceleration responses in time domain

Figure 14 collects both the maximum horizontal and vertical absolute acceleration values of the SMR C.G., indicated in Figure 9, taken from each simulation. Results relevant to the SMR endowed with the LM, FPD, and RF are presented, and median values are also depicted with horizontal lines. As anticipated, in the case of horizontal accelerations, both the proposed LM and FPD perform similarly with regard to the RF; nonetheless, in the vertical direction, the performance of the LM is far superior to the FPD solution for each seismic record. More precisely, in terms of median values, the LM solution reduces the peak vertical
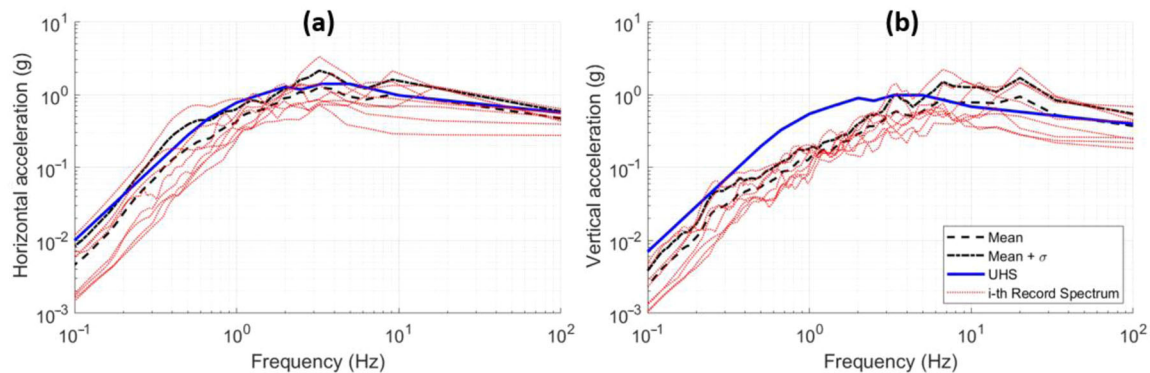
FIGURE 13 Mean and response spectra of the selected accelerograms and spectra plus one standard deviation spectra for the UHS of Priolo Gargallo: (a) horizontal component; (b) vertical component

accelerations by almost 50% with regard to the RF case, while the FPD solution exhibits an increased value of 12%.

The adoption of QZS layers introduces significant vertical flexibility and causes a possible rocking motion and high displacements or accelerations of the SMR edges/corners. As highlighted by Medel-Vera and Ji (2015) when vertical flexibility is introduced, rocking suppression systems may be required. Also, Domaneschi et al. (2012) concluded that rocking effects lead to significant variations of vertical forces that may affect the design of isolators. Clearly, these effects are also possible in the case of QMs due to the favorable vertical flexibility. Thus, as the distance from the C.G. increases, the rocking may cause undesirable additional vertical motions. In the case of the SMR to hand, this distance can reach up to 38.2 m. To dispel any doubts on this aspect, Figure 15 depicts both median peak vertical and horizontal acceleration values of the C.G. and the upper-west corner shown in Figure 9. The benefits in terms of absolute accelerations provided by the QZS layers are evident in all cases. The most favorable performance in the vertical direction is provided by the QM-B2 solution, in which the acceleration is reduced up to 21% for LM and 11% for RF. When the corner accelerations are perused, a substantial increase is observed for the FPD and the RF solutions in both directions; more precisely, 0.05 rad/s^2 and 0.09 rad/s^2 rotational acceleration values are tracked. Relevant values reduce to 0.02 rad/s^2 for the LM case due to the rocking suppression of the resonators. Further improvements are achieved with the single-layer QZS cases, that is, QM-B1 and QM-T1, which exhibit a rotational acceleration value of 0.01 rad/s^2. In addition, both QM-B2 and QM-T1B1 solutions exhibited rotational acceleration values similar to those of the LM solution. Clearly, the excessive flexibility in the vertical direction causes the resonators not to be able to suppress excessive rocking motions.

The best performance at the corner of the SMR is observed by the use of the QM-B1 case; while a signifi-

cant improvement with regard to to the FPD solution is observed with the LM due to the difference in rotational acceleration.

6.4 | Displacement responses in time domain

To further understand the dynamics of the metafoundations, peak displacement values of the C.G. were evaluated. Relevant results are presented in Figure 16, where the contribution of each layer to the median peak displacement can be appreciated.

The distributions allow for understanding the effects of the QZS layer location with regard to the horizontal displacement; all the proposed metafoundations performed better than the FPD foundation, and the most favorable performance is reached with the QM-B2 solution. Conversely, the maximum vertical displacement is observed with the QM-B2 solution; in fact, the QM-B2 metafoundation transfers input energy from horizontal to vertical motion by means of rotational coupling of DoFs. Moreover, the QZS layers exhibit limited movement in the horizontal direction.

Concerning the vertical displacements of the C.G., both LM and FPD exhibit similar absolute displacement with regard to ground. However, it can be observed that the FPD solution entails more relative vertical displacements on the SMR building. When QZS layers are introduced, a significant vertical displacement increase of the C.G. is observed up to 12.8 mm. Evidently, the vertical flexibility introduced causes significant acceleration of the isolated solution. The localization of the dynamic modes in the flexible layer (Chandrashaker et al., 2016) generally contributes to a large fraction of the displacement response.

The importance of the QZS layer location can be again understood from Figure 16; while both QM-B1 and QM-T1

TABLE 7 List of selected recorded accelerograms (PGV: peak ground velocity; PGD: peak ground displacement)

Earthquake name	Station	Mw	Rjb (km)	Vs30 (m/s)	Horizontal PGA (cm/s²)	Horizontal PGV (cm/s)	Horizontal PGD (cm)	Vertical PGA (cm/s²)	Vertical PGV (cm/s)	Vertical PGD (cm)
Erzincan, 1992	MM	6.6	13.0	421	381.4	101.3	26.2	242.9	15.6	37.3
South Iceland, 2000	Kaldarholt	6.5	7.0	–	613.6	38.9	4.1	654.1	20.0	13.3
South Iceland, 2000	Solheimar	6.4	11.0	–	412.3	37.5	15.0	411.8	23.7	5.8
L'Aquila, 2009	AQA	6.3	4.6	549	433.8	26.6	3.6	435.4	9.4	1.7
L'Aquila, 2009	AQG	6.3	4.4	696	479.3	35.7	4.4	234.6	10.4	1.9
L'Aquila, 2009	AQV	6.3	4.9	474	535.2	42.7	3.3	486.7	12.4	2.5
Landers, 1992	Joshua tree	7.3	11.0	379	268.8	30.4	121.9	177.6	14.7	6.1
Northridge-01, 1994	Castaic	6.7	20.1	450	557.2	51.7	9.6	212.9	12.2	5.1

experience similar horizontal displacements, QM-T1 exhibits 30% less vertical displacement than that of QM-B1. Moreover, the localization effect in the QM-T1 is lower as the linear layer also displaces more. Since the QZS does not affect the linear layer, this can be related to the limited motion of the resonators. These results can be compared with the acceleration values depicted in Figure 15. The low vertical displacement causes high acceleration values and points out that the QM-T1 solution is stiffer than the QM-B1 solution.

The effect of the location of the QZS layer on the behavior of resonators can be appreciated in Figure 17, where the median peak vertical displacements of resonators are shown. The x-axis defines the jth resonator depicted in Figure 9; subsequently, $j = 1$ defines the leftmost resonator, and $j = 15$ identifies the rightmost one. LM and QM cases entail resonator horizontal displacement values in the range 100–130 mm; consequently and for brevity, they are not presented. First, the introduction of the QZS layers significantly increases the vertical motion range of resonators, which causes an energy dissipation increase. When the QZS layer is placed at the bottom, substantial vertical motion differences occur between the outer and inner resonators; this behavior proves the existence of rocking motions, and therefore the QSZ layers must be properly used. In the case of the QM-1B metafoundation, the main cells of the linear layer exhibit low displacements, but the resonators significantly move to suppress rocking and a reduction of accelerations at the corners of the SMR. Conversely, the difference between the motion of the resonators is quite limited in the QM-T1 case; this behavior means that linear layers do not work against rocking motions but rather against vertical motions. Owing to its excessive flexibility, the QM-B2 case entails excessive resonator motions in a high displacement range; as such, the wanted rocking suppression is limited.

For completeness, it is deemed necessary to provide some information about the costs of both innovative and standard isolation solutions. For brevity, this information has been detailed in Tables A1–A3 of the Appendix. A comparison between the estimated costs of the optimized LM, that is, 5.78 million euros and a standard isolation solution made with the FPD, that is, 5.46 million euros, entails that costs are comparable. Nonetheless, the costs associated with FPD do not take into account the needed protection of the SMR against the vertical component of an earthquake (Y.-N. Huang et al., 2016; Schellenberg et al., 2015). In this situation, more complex and expensive isolators (Fukasawa et al., 2019) or a strong SMR superstructure must be considered.
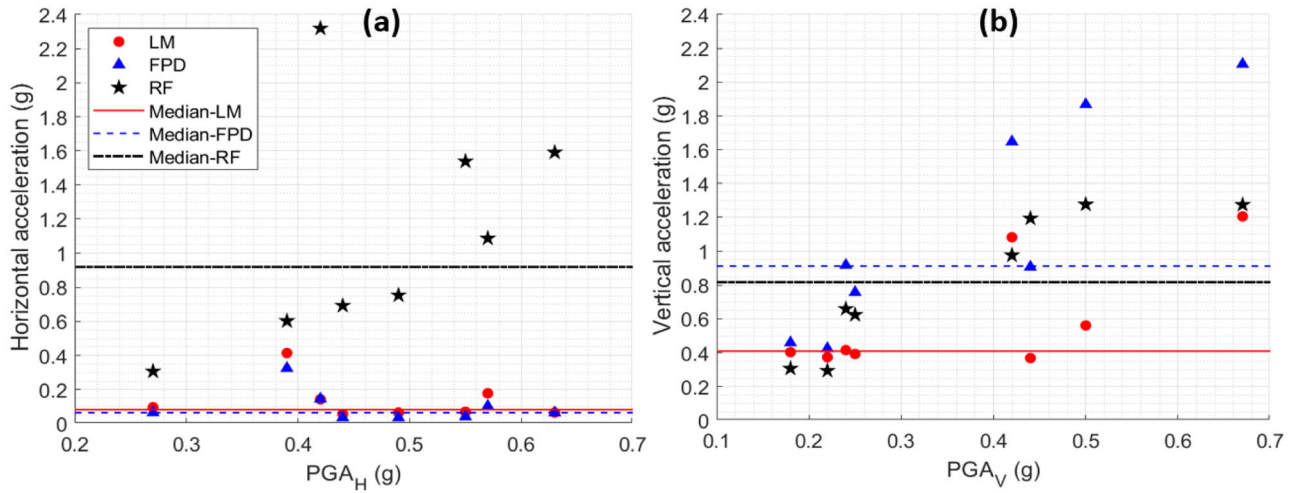
FIGURE 14 Peak acceleration results for the C.G. of the SMR building regarding PGA of accelerograms and median values: (a) horizontal acceleration, (b) vertical acceleration (LM: linear metafoundation, FPD: friction pendulum devices, RF: rigid foundation)
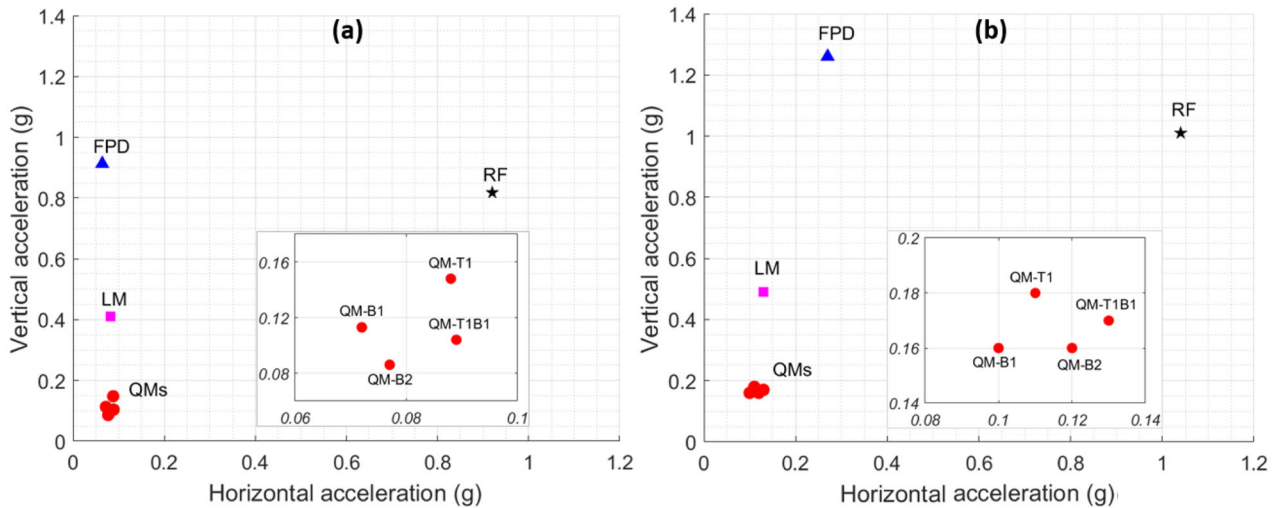

FIGURE 15 Median of horizontal–vertical peak acceleration results for the: (a) C.G., (b) upper-west corner of the SMR building. (QM: Metafoundations with QZS layers)
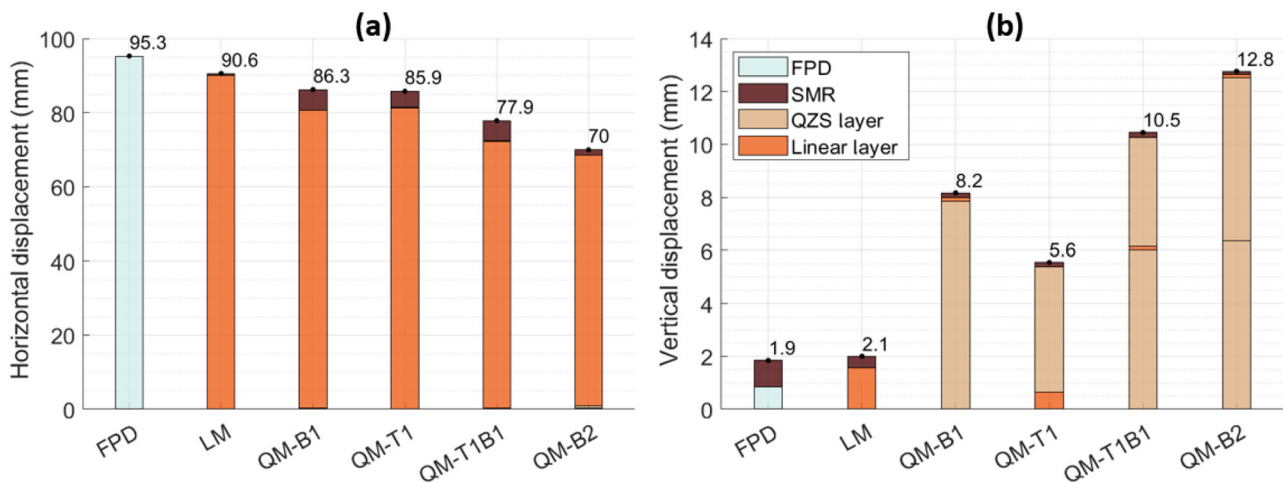

FIGURE 16 Median of the peak displacement of the SMR's C.G.: (a) horizontal component, (b) vertical component
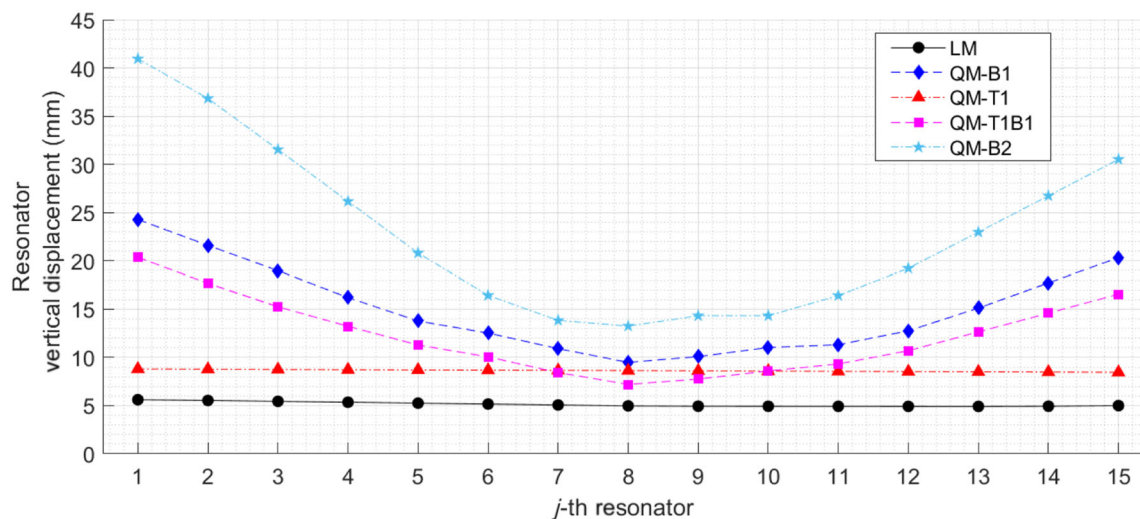
FIGURE 17 Median of the peak vertical displacements of the jth resonator where j is given in Figure 9

7 | CONCLUSION

SMRs are under development and investigation around the world because they exhibit many attractive features capable of improving the safety and reliability of operations. Along this main vein, this paper aimed to investigate in depth the seismic mitigation of a typical SMR. Extreme loading conditions relevant to the SSE were considered; and a detailed structural model was synthesized to reproduce the main dynamic properties of the SMR, also taking into account the reactor pools. Then, to protect the reactor from strong earthquakes, two types of metafoundations were conceived and developed. More precisely: (i) an LM endowed with multiple linear cells, and (ii) several metafoundation configurations, QMs, equipped with a single layer of linear cells and some layers that consist of vertical QZS cells, which provided additional flexibility and dissipation against symmetrical and nonsymmetrical modes of the coupled system.

In both cases, it was shown that the metafoundation can be optimized via the dynamic properties of the resonators in terms of horizontal and vertical stiffness and damping, also including the stochastic nature of seismic events. For an effective optimization that involved a multivariate multi-objective problem, a novel two-steps procedure was proposed: (i) a global sensitivity analysis with a parameter grouping strategy with the WSM, where the optimization problem with multiple variables was broken into multiple suboptimization problems with fewer variables, and a single objective; (ii) a step where each subproblem was solved using the proposed recursive GrSS. The performance of the procedure was compared with state-of-the-art algorithms; hence, high accuracy with a limited number of function evaluations was achieved. In addition, the suggested procedure provides global sensitivity of parameters that is beneficial for decision-making.

Subsequently, the optimized metafoundations were examined by means of frequency response and time history seismic analyses; and relevant results were compared both with SMR endowed with a RF and standard base-isolated solutions. It can be concluded that the LM is able to isolate the SMR building against horizontal excitations like the conventional base-isolated solutions; however, the LM can also mitigate vertical accelerations. With the introduction of the QZS layers, the isolation performance of the LM to vertical excitations is significantly improved. Furthermore, the location of the QZS layer(s) also affects the system response. The best performance indeed is obtained by using a single QZS layer below the linear layer in which the acceleration was reduced up to 11 % with regard to the RF case. It was also demonstrated that the existence of multiple resonators significantly prevents rocking motions due to their effectiveness with regard to the distance from the C.G. of the SMR.

In general terms, it is worthy to emphasize that the proposed metafoundations are characterized by simplicity and modularity: They can be easily adapted to protect different types of SMRs and other components of NPPs such as tanks and auxiliary buildings. Moreover, to enhance the understanding of these coupled systems, the validation and further investigations of wire ropes and QZS elements by means of 3D hysteretic experimental characterization, comprising soil-structure interaction, are required. Finally, to perform reliability evaluations, both geometrical and mechanical randomness need to be included.

REFERENCES

Aldwaik, M., & Adeli, H. (2014). Advances in optimization of highrise building structures. *Structural and Multidisciplinary Optimization*, *50*(6), 899–919.

Alessandri, S., Giannini, R., Paolacci, F., & Malena, M. (2015). Seismic retrofitting of an HV circuit breaker using base isolation with wire ropes. Part 1: Preliminary tests and analyses. *Engineering Structures*, *98*, 251–262.

Amezquita-Sanchez, J. P., Park, H. S., & Adeli, H. (2017). A novel methodology for modal parameters identification of large smart structures using MUSIC. *Empirical Wavelet Transform, and Hilbert Transform, Engineering Structures*, *147*, 148–159.

ASCE/SEI. (2016). Seismic analysis of safety-related nuclear structure*s*. American Society of Civil Engineers.

Anawat, S., Shuto, N., Imamura, F., Koshimura, S., Mas, E., & Yalciner, A. C. (2013). Lessons learned from the 2011 Great East Japan Tsunami: Performance of Tsunami countermeasures, coastal buildings, and Tsunami evacuation in Japan. *Pure and Applied Geophysics*, *170*, 993–1018.

Benefits NuScale Power. (2022). https://www.nuscalepower.com/benefits

Basone, F., Wenzel, M., Bursi, O. S., & Fossetti, M. (2019). Finite locally resonant Metafoundations for the seismic protection of fuel storage tanks. *Earthquake Engineering and Structural Dynamics*, *48*(2), 232–252. https://doi.org/10.1002/eqe.3134

Basone, F., Bursi, O. S., Aloschi, F., & Fischbach, G. (2021). Vibration mitigation of an MDoF system subjected to stochastic loading by means of hysteretic nonlinear locally resonant metamaterials. *Scientific Reports*, *11*, 9728. https://doi.org/10.1038/s41598-021-88984-0

Bursi, O. S., Basone, F., & Wenzel, M. (2021). Stochastic analysis of locally resonant linear and hysteretic metamaterials for seismic isolation of process equipment. *Journal of Sound and Vibration*, *510*, 116263. https://doi.org/10.1016/j.jsv.2021.116263

Carrella, A., Brennan, M. J., & Waters, T. P. (2007). Static analysis of a passive vibration isolator with quasi-zero-stiffness characteristic. *Journal of Sound and Vibration*, *301*(3-5), 678–689. https://doi.org/10.1016/j.jsv.2006.10.011

Carrella, A., Brennan, M. J., Kovacic, I., & Waters, T. P. (2009). On the force transmissibility of a vibration isolator with quasi-zero-stiffness. *Journal of Sound and Vibration*, *322*(4-5), 707–717. https://doi.org/10.1016/j.jsv.2008.11.034

Chandrashaker, A., Adhikari, S., & Friswell, M. I. (2016). Quantification of vibration localization in periodic structures. *ASME Journal of Vibration and Acoustics*, *138*(2), 021002. https://doi.org/10.1115/1.4032032

Chang, Y. (2009). N-dimension golden section search: Its variants and limitations. *2009 2nd International Conference on Biomedical Engineering and Informatics*, Tianjin, China (pp. 1–6). https://doi.org/10.1109/BMEI.2009

Chopra, A. K. (2017). *Dynamics of structures*. Pearson.

Clough, R. W., & Penzien, J. (2003). *Dynamics of structures*. CSI Computers & Structures, Inc.

Computers and Structures, Inc. (CSI). (2022). SAP2000: Integrated finite element analysis and design of structures (Version 23.3.1) [Software]. SAP2000.

Domaneschi, M., Martinelli, L., & Perotti, F. (2012). The effect of rocking excitation on the dynamic behaviour of a Nuclear Power Plant reactor building with base isolation. *Proceedings of the 15th World Conference on Earthquake Engineering*, Lisbon, Portugal.

El-Khoury, O., & Adeli, H. (2013). Recent advances on vibration control of structures under dynamic loading. *Archives of Computatational Methods in Engineering*, *20*, 353–360. https://doi.org/10.1007/s11831-013-9088-2

European Committee for Standardization. (2004a). Design of composite steel and concrete structures. Part 1-1: General rules and rules for buildings. *Eurocode 4-1-1, CEN/TC*, *250*, Brussels.

European Committee for Standardization. (2004b). Design of structures for earthquake resistance. Part 1: General rules, seismic actions and rules for buildings. *Eurocode 8-1, CEN/TC*, *250*, Brussels.

European Committee for Standardization. (2005a). Design of composite steel and concrete structures. Part 1–2: General rules - Structural fire design regulation. *Eurocode 4-1-2, CEN/TC*, *250*, Brussels.

European Committee for Standardization. (2005b). Design of steel structures. Part 1-1: General rules and rules for buildings. *Eurocode 3-1-1, CEN/TC*, *250*, Brussels.

FIPMEC. (2022). *Antiseismic devices* https://www.fipmec.it/it/prodotti/dispositivi-antisismici/ (in Italian)

Franchini, A., Bursi, O. S., Basone, F., & Sun, F. (2020). Finite locally resonant metafoundations for the protection of slender storage tanks against vertical ground accelerations. *Smart Materials and Structures*, *29*(5), 055017. https://doi.org/10.1088/1361-665X/ab7e1d

Fukasawa, T., Okamura, S., Somaki, T., Miyagawa, T., Uchita, M., Yamamoto, T., Watakabe, T., & Fujita, S. (2019). Research and development of three-dimensional isolation system for sodium-cooled fast reactor: Part 4–proposal of optimal combination method for disc spring units and newly friction model for sliding elements. *American Society of Mechanical Engineers, Pressure Vessels and Piping Division (Publication) PVP*, San Antonio, TX. https://doi.org/10.1115/PVP2019-93480

Furuta, K., & Kanno, T. (2017). How the Fukushima Daiichi accident changed (or not) the nuclear safety fundamentals? In J. Ahn, F. Guarnieri, & K. Furuta (Eds.), *Resilience: A new paradigm of nuclear safety*. Springer.

Golub, G. H., & Van Loan, C. F. (2012). *Matrix computations* (Vol. 3). The Johns Hopkins University Press.

Graham, E. W., & Rodriguez, A. M. (1952). The characteristics of fuel motion which affect airplane dynamics. *Journal of Applied Mechanics*, *19*(3), 381–388. https://doi.org/10.1115/1.4010515

Gutierrez Soto, M., & Adeli, H. (2018). Vibration control of smart base-isolated irregular buildings using neural dynamic optimization model and replicator dynamics. *Engineering Structures*, *156*, 322–336.

Hooke, R., & Jeeves, T. (1961). Direct search solution of numerical and statistical problems. *Journal of the ACM*, *8*, 212–229. https://doi.org/10.1145/321062.321069

Huang, X., Liu, X., Sun, J., Zhang, Z., & Hua, H. (2014). Vibration isolation characteristics of a nonlinear isolator using euler buckled beam as negative stiffness corrector: A theoretical and experimental study. *Journal of Sound and Vibration*, *333*(4), 1132–1148. https://doi.org/10.1016/j.jsv.2013.10.026

Huang, Y.-N., Whittaker, A. S., & Luco, N. (2011a). A probabilistic seismic risk assessment procedure for nuclear power plants: (I) Methodology. *Nuclear Engineering and Design*, *241*, 3996–4003.

Huang, Y.-N., Whittaker, A. S., & Luco, N. (2011b). A probabilistic seismic risk assessment procedure for nuclear power plants: (II) Application. *Nuclear Engineering and Design*, *24*, 3985–3995.

Huang, Y.-N., Yen, W.-Y., & Whittaker, A. S. (2016). Correlation of horizontal and vertical components of strong ground motion for response-history analysis of safety-related nuclear facilities. *Nuclear Engineering and Design*, *310*, 273–279.

IAEA, International Atomic Energy Agency. (2014). *Advances in small modular reactor technology developments*. International Atomic Energy Agency.

IAEA, International Atomic Energy Agency. (2016). *Design safety considerations for water cooled small modular reactors incorporating lessons learned from the Fukushima Daiichi accident*. IAEA-TECDOC-1785. International Atomic Energy Agency.

Janon, A., Klein, T., Lagnoux-Renaudie, A., Nodet, M., & Prieur, C. (2014). Asymptotic normality and efficiency of two Sobol index estimators. *ESAIM: Probability and Statistics*, *18*, 342–364. https://doi.org/10.1051/ps/2013040

Japan Electric Association. (2013). *Technical guidelines on seismic base isolated system for structural safety and design of nuclear power plants*. JEAG 4614-2013, Japan.

Kanai, K. (1957). Semi-empirical formula for the seismic characteristics of the ground. *Bulletin of the Earthquake Research Institute, University of Tokyo*, *35*(2), 309–325. https://doi.org/10.15083/0000033949

Kicinger, R., Arciszewski, T., & De Jong, K. (2005). Evolutionary computation and structural design: A survey of the state-of-the-art. *Computers & Structures*, *83*(23-24), 1943–1978.

Kelly, J. M. (1990). Base isolation: Linear theory and design. *Earthquake Spectra, 1990*, *6*(2), 223–244.

Kramer, S. L. (1996). *Geotechnical earthquake engineering*. Prentice Hall. http://www.worldcat.org/isbn/0133749436

Lin, S., Zhang, Y., Liang, Y., Liu, Y., Liu, C., & Yang, Z. (2021). Bandgap characteristics and wave attenuation of metamaterials based on negative-stiffness dynamic vibration absorbers. *Journal of Sound Vibration*, *502*, 116088. https://doi.org/10.1016/j.jsv.2021.116088

Liu, X., Huang, X., & Hua, H. (2013). On the characteristics of a quasi-zero stiffness isolator using Euler buckled beam as negative stiffness corrector. *Journal of Sound and Vibration*, *332*(14), 3359–3376. https://doi.org/10.1016/j.jsv.2012.10.037

Marler, R. T., & Arora, J. S. (2010). The weighted sum method for multi-objective optimization: New insights. *Structural and multidisciplinary optimization*, *41*(6), 853–862.

Medel-Vera, C., & Ji, T. (2015). Seismic protection technology for nuclear power plants: A systematic review. *Journal of Nuclear Science and Technology*, *52*(5), 607–632. https://doi.org/10.1080/00223131.2014.980347

Mu, D., Shu, H., Zhao, L., & An, S. (2020). A review of research on seismic metamaterials. *Advanced Engineering Materials*, *22*, 1901148. https://doi.org/10.1002/adem.201901148

Muhammad & Lim, C. W. (2022). From photonic crystals to seismic metamaterials: A review via phononic crystals and acoustic metamaterials. *Archives of Computational Methods in Engineering*, *29*, 1137–1198. https://doi.org/10.1007/s11831-021-09612-8

Najafijozani, M., Becker, T. C., & Konstantinidis, D. (2020). Evaluating adaptive vertical seismic isolation for equipment in nuclear power plants. *Nuclear Engineering and Design*, *358*, 110399. https://doi.org/10.1016/j.nucengdes.2019.110399

Nelder, J. A., & Mead, R. A. (1965). Simplex method for function minimization. *The Computer Journal*, *7*(4), 308–313. https://doi.org/10.1093/comjnl/7.4.308

Park, J. W., & Seol, W.-C. (2016). Considerations for severe accident management under extended station blackout conditions in nuclear power plants. *Progress in Nuclear Energy*, *88*, 245–256.

Parsi, S. S., Lal, K. M., Kosbab, B. D., Ingersoll, E. D., Shirvan, K., & Whittaker, A. S. (2022). Seismic isolation: A pathway to standardized advanced nuclear reactors. *Nuclear Engineering and Design*, *387*, 111445.

Paya, I., Yepes, V., González-Vidosa, F., & Hospitaler, A. (2008). Multiobjective optimization of concrete frames by simulated annealing. *Computer Aided Civil and Infrastructure Engineering*, *23*(8), 596–610.

Ruy, W. S., Yang, Y. S., Kim, G. H., & Yeun, Y. S. (2001). Topology design of truss structures in a multicriteria environment. *Computer Aided Civil and Infrastructure Engineering*, *16*, 246–258.

Sarma, K. C., & Adeli, H. (1998). Cost optimization of concrete structures. *Journal of Structural Engineering*, *124*(5), 570–578.

Schellenberg, A. H., Sarebanha, A., Schoettler, M. J., Mosqueda, G., Benzoni, G., & Mahin, S. A. (2015). *Hybrid simulation of seismic isolation systems applied to an APR-1400 nuclear power plant*. PEER Report 2015/05, UC Berkeley.

Shafahi, Y., & Bagherian, M. (2013). A customized particle swarm method to solve highway alignment optimization problem. *Computer Aided Civil and Infrastructure Engineering*, *28*(1), 52–67.

Shi, X., Zhao, F., Yan, Z., Zhu, S., & Li, J.-Y. (2021). High-performance vibration isolation technique using passive negative stiffness and semiactive damping. *Computer Aided Civil and Infrastructure Engineering*, *36*(8), 1034–1055.

Synolakis, C., & Kânoğlu, U. (2018). The Fukushima accident was preventable. *Philosophical Transactions: Mathematical, Physical and Engineering Sciences*, *373*(2053), 1–23.

Sobol, I. M. (1993). Sensitivity estimates for nonlinear mathematical models. *Mathematical Modelling and Computational Experiments*, *4*, 407–414.

Stevenson, J. D. (2014). Summary of the historical development of seismic design of nuclear power plants in Japan and in the US. *Nuclear Engineering and Design*, *269*, 160–164.

Upadhyay, A. K., & Jain, K. (2003). Modularity in nuclear power plants: A re- view. *Journal of Engineering, Design and Technology*, *14*(3), 526–542.

U.S. Nuclear Regulatory Commission. (2015). *NUREG/CR-7193. Evaluations of NRC seismic-structural regulations and regulatory guidance, and simulation-evaluation tools for applicability to small modular reactors (SMRs)*. United States Nuclear Regulatory Commission, Office of Nuclear Regulatory Research.

U.S. Nuclear Regulatory Commission. (2007). *Regulatory guide 1.61: Damping values for seismic design of nuclear power plants*. US Nuclear Regulatory Commission.

Veletsos, A. S., & Tang, Y. (1986). Dynamics of vertically excited liquid storage tanks. *Journal of Structural Engineering*, *112*(6), 1228–1246. https://doi.org/10.1061/(ASCE)0733-9445(1986)112:6(1228)

Wenzel, M., Bursi, O. S., & Antoniadis, I. (2020). Optimal finite locally resonant metafoundations enhanced with nonlinear negative stiffness elements for seismic protection of large storage tanks. *Journal of Sound and Vibration*, *483*, 115488. https://doi.org/10.1016/j.jsv.2020.115488

Witarto, W., Wang, S. J., Yang, C. Y., Nie, X., Mo, Y. L., Chang, K. C., Tang, Y., & Kassawara, R. (2018). Seismic isolation of small modular reactors using metamaterials. *AIP Advances*, *8*(4), 045307. https://doi.org/10.1063/1.5020161

Witarto, W., Wang, S. J., Yang, C. Y., Wang, J., Mo, Y. L., Chang, K. C., & Tang, Y. (2019). Three-dimensional periodic materials as seismic base isolator for nuclear infrastructure. *AIP Advances*, *9*(4), 045014. https://doi.org/10.1063/1.5088609

Zhao, C., Yu, N., Peng, T., Lippolis, V., Corona, A., & Mo, Y. L. (2019). Study on the dynamic behavior of isolated AP1000 NIB under mainshock-aftershock sequences. *Progress in Nuclear Energy*, *119*, 103144.

Zhou, J., Wang, X., Xu, D., & Bishop, S. (2015). Nonlinear dynamic characteristics of a quasi-zero stiffness vibration isolator with cam–roller–spring mechanisms. *Journal of Sound and Vibration*, *346*, 53–69.

APPENDIX

The costs associated with the LM can be divided into two parts relevant to variable costs and fixed costs. The variable costs correspond to materials or work items that are subjected to notable changes in the LM height H. Conversely, the fixed costs are independent of H. The items that contribute to the variable costs of the LM are collected in Table A1 for H = 9.5 m. Table A2 instead gathers the fixed cost items. With the inclusion of the fixed costs, the total cost of the considered design solution was estimated to be about 5.78 million euros.

For the sake of comparison, also the costs relevant to an SMR isolated with standard FPDs are estimated. They can be deduced from Table A3 and read as 5.46 million euros; they are further commented on in Section 6.4. It is just underlined here that the apparently cheaper FPD solution does not protect the SMR against the vertical component of an earthquake.

TABLE A1 Costs of the LM related to items that vary with the height (H = 9.5 m)

Material or work	Quantity	Unit	Unit cost	Total cost
Column (steel)	516,298	kg	1 €/kg	€516,298
Column (reinforced concrete [RC])	673	m^3	250 €/m^3	€168,250
Resonator (RC)	13,392	m^3	230 €/m^3	€3,080,160
Excavation	26,208	m^3	20 €/m^3	€524,160
			Total	**€4,288,868**

TABLE A2 Costs of the LM related to items that do not depend on the height

Material or work	Quantity	Unit	Unit cost	Total cost
Main slab	2496	m3	250 €/m^3	€624,000
Foundation	2496	m3	230 €/m^3	€574,080
Wire ropes	48,960	kg	6 €/kg	€293,760
Maintenance	0	Per lifetime	0	€–
			Total	**€1,491,840**

TABLE A3 Costs of the standard isolated solution friction pendulum device (FPD)

Material or work	Quantity	Unit	Unit cost	Total cost
FPD unit	90	unit	€3500	€315,000
Column (RC)	1323	m^3	250 €/m^3	€330,625
Excavation	14,976	m^3	20 €/m^3	€299,520
Main slab	6240	m^3	250 €/m^3	€1,560,000
Foundation	6240	m^3	230 €/m^3	€1,435,200
Maintenance	9	Per lifetime	135,000€	€1,417,500
Fire protection	–	–	100,000€	€100,000
			Total	**€5,457,845**